EGG-2511
Distribution Category: UC-66a

EGG--2511

DE87 012847

GEOTHERMAL INJECTION TECHNOLOGY PROGRAM ANNUAL PROGRESS REPORT: FISCAL YEAR 1986

Prepared By:

Idaho National Engineering Laboratory
and
University of Utah Research Institute

Published July 1987

Prepared for the
U.S. Department of Energy
Idaho Operations Office
Under DOE Contract No. DE-AC07-761D01570

DISCLAIMER

ABSTRACT

This report summarizes the Geothermal Injection Technology Program major activities in fiscal year 1986. The Idaho Engineering Laboratory (INEL) and the University of Utah Research Institute (UURI) have been conducting injection research and testing for this program, which was initiated in 1983. Activities at the INEL, representative element modeling of fracture systems based on stochastic analysis, dual permeability modeling of flow in a fractured geothermal reservoir, and dual permeability model - laboratory and FRACSL-validation studies, are presented first, followed by the University of Utah Research Institute tracer development - experimental studies, which includes a brief description of activities planned for FY-1987.

CONTENTS

FIGURES

TABLES

NOMENCLATURE

A	cross-sectional area
a	depth of fracture into the plane of the element
b	average (expected) aperture
b	fracture aperture
c	concentration
c_o	initial tracer concentration
c(z,t)	solute concentration as a function of z and t
D_l	dispersion coefficient
D_m	diffusion coefficient
erfc	complimentary error function
g	gravitational acceleration
k	hydraulic conductivity
ln	natural logarithm
p( )	probability density function
Pe	peclet number
Q	flow rate
t	time
t	average transit time across an element
T	length of the element, in z direction
v	average velocity of fluid in a fracture
V_i	injected volume
V_p	pore volume
W	width of the element, normal to fracture faces
x	distance along a fracture
z	distance across an element in the z direction
Z	position of fracture centers on the z axis
α	dispersivity length
ρ	fluid density
λ_ℓ	expected length of l
λ_z	average spacing of fracture centers in the z direction
λ_s	average spacing of fracture centers normal to the fracture faces
ϕ	pressure
σ^2	variance of ln(b)
σ_t^2	variance of transit time across an element
ε	proportionality constant between aperature and fracture length
β	proportionality constant between average aperature and fracture length
γ	ratio of velocity at a transverse position in a fracture to the mean velocity
ℓ	length of a fracture
μ	absolute viscosity
< >	expectation operator
δ( )	delta function

GEOTHERMAL INJECTION TECHNOLOGY PROGRAM

1. INTRODUCTION

The injection of geothermal fluids is considered one of the primary concerns currently facing geothermal developers. Injection is used to dispose of the large volumes of spent geothermal fluids associated with power generation and direct use developments, to offset reservoir depletion and to reduce the risk of subsidence. However, injection can cause early thermal breakthrough with a consequent reduction in enthalpy, loss of injectivity due to chemical interactions in the reservoir, scaling and corrosion in injection piping and wells, aquifer contamination, and induced seismicity.

Selecting locations for injection wells and planning well-field operations to optimize thermal recovery from a geothermal reservoir require the ability to assess the benefits of injection against potential negative thermal, chemical, and physical impacts. Fractures are important features in most geothermal reservoirs and can be critical parameters in thermal breakthrough. Consequently, this assessment cannot be accomplished using standard reservoir engineering techniques that are based on homogeneous porous media.

Since 1983, the University of Utah Research Institute (UURI) and the Idaho National Engineering Laboratory (INEL) have been conducting injection research and testing sponsored by the U.S. Department of Energy (DOE), Geothermal Technology Division. The objective of this research and testing is to develop a better understanding of fluid migration in fractured geothermal reservoirs during injection. The techniques developed will be used to predict the fate of injected fluids and to improve field testing and data interpretation procedures for application by the geothermal industry.

The emphasis of the INEL/UURI research programs is on tracer techniques to evaluate fluid migration in geothermal reservoirs. The relationship between fluid/tracer transport and reservoir parameters forms the basis for evaluating heat recovery and for predicting thermal breakthrough in a reservoir. These predictions can then be used to plan well placements and well-field operations to optimize resource recovery.

The INEL/UURI programs combine laboratory experimentation, computer simulation, and field testing in the study of injected fluid migration. Methods of interpreting data are refined by relating observable phenomena (pressure response, fluid temperature, tracer breakthrough) to reservoir characteristics. Parametric studies are performed using numerical simulation codes to determine the sensitivity of measurable parameters to changes in reservoir conditions. Codes are verified against analytical solutions and are validated using laboratory models. The laboratory validation step provides assurance that the codes represent the transport processes properly.

Much of the research performed in 1986 centered around the use of a code to simulate flow and transport in fractured media. The code is called FRACSL from its fractured media orientation. The code simulates fractures as individual (discrete) elements inbedded in a porous matrix material. The two distinct behaviors of discrete elements and continuous porous elements have led to a description of dual permeability for this type of approach. Transport processes are simulated in FRACSL through the use of direct simulation, which represents a distributed process by the movement of discrete marker particles of information.

Unique analytical techniques and capabilities have been developed to support injection research. The interdisciplinary staff of earth scientists, physicists and engineers, and the laboratory facilities dedicated to this research represent a broad range of technological resources and experience.

1.1 Transport Processes

A sound theoretical understanding of the processes that control mass, heat and solute transport through fractured rocks is necessary to understand how geothermal reservoirs will respond to fluid injection. Laboratory models have been used to collect data under controlled conditions for validation of simulation codes. This validation step assists in separating uncertainty in code parameters from uncertainty in reservoir geometry. While laboratory models cannot provide a totally realistic representation of a geothermal reservoir, observing flow and transport in the laboratory, and describing them mathematically in a code, does provide significant insight into these processes that cannot be gained in the field.

In previous years, an algorithm for transport in fractures was developed and incorporated into the two-dimensional flow and transport code FRACSL. The code has been verified against analytical solutions for flow and transport in porous media and in single fractures. The code has also been validated for flow and transport in complex fracture systems using a laboratory model. The tests demonstrated that assuming complete mixing of tracer at fracture intersections is not justified. Homogenization of tracer concentrations in

fractures in geothermal reservoirs will depend on fracture system geometry and local flow rates.

1.2 Data Interpretation

Ongoing research at the INEL is aimed at developing methods to interpret reservoir and tracer data from fractured geothermal reservoirs. Reservoir engineering analyses are generally based on either analytical solutions to an idealized reservoir configuration (type-curve matching) or on distributed parameter simulation techniques. Because of the complexity of fractured geothermal reservoirs, the INEL program emphasizes the latter approach. Adding the capability to match tracer response curves to the ability to match pressure and temperature data allows the study of phenomena that affect both solute and thermal transport. Predicting the response to tracer injection, then, indicates an ability to predict thermal responses to injection.

The FRACSL flow and transport code has been developed for reservoirs where both fracture and matrix permeability are important. FRACSL simulates tracer transport in a reservoir using a particle tracking algorithm. The code has been validated against analytical solutions for flow and transport in porous media. Correlation of tracer testing conducted at the East Mesa known geothermal resource area (KGRA), Imperial Valley, California geothermal field demonstrated the utility of the code. Results from the analysis of tracer data collected at East Mesa quantified the dispersion characteristics of the reservoir, natural flow rates, and the ratio of maximum to minimum hydraulic conductivities.

A three-dimensional simulation of injection-production tests at the Raft River, Idaho geothermal field was performed using a statistical description of the fracture system. Interpretation of wellbore logs and televiewer data identified three primary fracture sets which were modeled in addition to a major hydraulic fracture intersecting the injection well.

Work was initiated in FY-86 on an innovative approach to dealing with complex fractured reservoirs. In complex reservoirs, it is impossible to deal with all the fractures explicitly in a computer code. The classic approach to this problem is to treat the fracture system as an equivalent continuum. This does not adequately deal with a wide range of fractures, nor does it treat local inhomogeneities, which can affect heat transfer and fluid migration in a reservoir. The INEL dual-permeability approach explicitly simulates the important fractures, while using an equivalent continuum approach for the smaller fractures and the matrix. A method of developing properties (permeability, tracer dispersivity) of the continuum elements has been proposed. This method, which is presented in Section 3, employs representative elements, which preserve the observed phenomenon that reservoir properties are a function of element size.

1.3 Tracer Development and Geochemistry

The full effect of injecting a relatively cool fluid into a geothermal reservoir cannot be modeled by only measuring temperature and pressure, which is the normal procedure for reservoir modeling. To effectively model injection, specific packets of fluid must be traced underground, and the temperature, pressure, timing, and saturation with response to mineral phases must be monitored.

Tracers can be used to monitor the movement of groundwaters and geothermal fluids, and can be used as a reference to quantify changes in fluid chemistry as a result of injection. Despite their potential importance to the geothermal operator, very few tracers are currently available. Little is known about their stability or behavior at the elevated temperatures that typify geothermal resources suitable for power generation.

During the past 3 years, UURI has been involved in tracer research and testing. Section 5 discusses details of laboratory research conducted on developing new tracers. The sulfonated and fluorinated hydrocarbons are a promising new class of tracers. They appear to exhibit good thermal stability and, because of the wide range of compositions, could be used to trace many wells simultaneously.

1.4 Field Testing

In FY-86, DOE initiated a series of cooperative field tests with industry. The objective of these tests is to provide field testing and validation of analytical and simulation techniques developed by research participants. These field tests demonstrate the utility and limits of application of the techniques and also provide effective technology transfer to the geothermal industry.

The first tests are scheduled to be conducted at Magma Power Company's reservoir at East Mesa and will be conducted by INEL, UURI, Stanford University, Lawrence Livermore National Laboratory, and Lawrence Berkeley Laboratory. Included in the testing program are:

- Nonisothermal transient injection tests—Studies of pressure transients during nonisothermal injection tests have shown that the data can be used to calculate reservoir permeability and well skin factor. Using the concept of a thermal-skin effect, the distance to the thermal front can be calculated.

This analytical technique assumes homogeneity and further research is required to apply the concept to heterogeneous geothermal reservoirs.

- Vertical seismic profiling—A vertical seismic profile survey will be conducted using multiple offset points around two deep injection wells. The data will be used to develop a velocity section, which will be combined with other geophysical interpretations to map faults and fracture zones.
- Well-to-well tracer tests—Well-to-well tracer injection and monitoring tests will be conducted to evaluate interpretive models developed to forecast thermal breakthrough. The data will be used to provide information on reservoir transport parameters (mean fluid velocity, significance of reservoir inhomogeneities, preferential transport directions). These tests will also be used to test the performance in the field of tracers being developed for geothermal environments.
- Spontaneous potential surveys—Research has been conducted in the application of spontaneous potential (SP) surveys to detect anomalies created by injection in geothermal fields. A detectable SP effect could provide data on the direction and rate of movement of the injected fluid front.

In support of these tests, existing geological, geophysical, and geochemical data will be reinterpreted using newly developed methods. The data will be used to compile a comprehensive model of the reservoir that will support the interpretations of data collected during the field tests.

1.5 Summary

Key accomplishments in FY-86 include the development and validation of a numerical code, simulating flow and transport in fractured reservoirs; the identification of hydrocarbon tracers which are thermally stable at temperatures representative of a large number of geothermal reservoirs in the United States; development of an innovative technique for quantifying reservoir parameters for complex fracture systems; and simulation in three dimensions of flow in the vicinity of a wellbore in a fractured geothermal reservoir. The remaining sections of this report provide details on the accomplishments for FY-86.

2. REPRESENTATIVE ELEMENT MODELING OF FRACTURE SYSTEMS BASED ON STOCHASTIC ANALYSIS

T. M. Clemo
Idaho National Engineering Laboratory

An important task associated with reservoir simulation is the development of a technique to model a large number of fractures with a single description. Representative elements must be developed before reservoir scale simulations can adequately address the effects of intersecting fracture systems on fluid migration. An effective element model would bring the complexity of large-scale simulations to manageable levels and reduce the cost. Stochastic analysis is a powerful tool, which can determine the hydraulic and transport characteristics of intersecting sets of statistically defined fractures.

Hydraulic and transport characteristics are required to develop representative elements. Given an assumption of fully developed laminar flow, the net fracture conductivities and, hence, flow velocities can be determined from descriptive statistics of fracture spacing, orientation, aperture, and extent. The distribution of physical characteristics about their mean leads to a distribution of the associated conductivities. The variance of hydraulic conductivity induces dispersion into the transport process.

The simplest of fracture systems, a single set of parallel fractures, is treated to demonstrate the usefulness of stochastic analysis. Explicit equations for conductivity of an element are developed and the dispersion characteristics are shown. The analysis reveals the dependence of the representative element properties on the various parameters used to describe the fracture system.

2.1 Introduction

This section addresses the development of representative element models to simulate a small portion of a fracture system, an area of reservoir modeling that has not had significant exposure in the literature. The main thrust is that, given a statistical description of a fracture system, a large number of fractures can be modeled with a single element. These elements can be combined with other elements and representations of individual fractures to form a reservoir scale simulation of manageable size and cost. The approach of combining both representative elements and discrete fractures has been given the term "dual permeability." A promising technique for deriving the properties of a representative element is the analytical reduction of statistical distributions into expected values. This technique is known as stochastic analysis.

Also provided is a brief background of current research in fractured reservoir modeling, followed by a discussion of what parameters may be needed to characterize a fracture system. The final portion is an example of using stochastic analysis to model a simple fracture geometry.

2.2 Background

Modeling of fractured media has been based on two primary approaches, continuum and discrete. These two approaches are briefly discussed below and compared to a third approach, which contains elements of both.

The continuum approach is based on a lumped parameter model of the fracture system, where the continuum is composed of representative elementary volumes. These volumes model the hydraulic and transport behavior of a large number of fractures. Representative elementary volumes are akin to representative elements but model the whole response of fracture systems rather than the connections between discrete fractures. For simulations of real fracture systems, the hydraulic and transport properties are determined from a statistical description of the fracture system. The elements must represent a fracture system large enough that effects of individual fractures cannot be distinguished in the response of the model. The scale must be large enough so that the fractured rock can be treated as if it were homogeneous. Consequently, reducing a large number of fractures to a single representation has become an active area of research (Dershowitz, 1984).

A homogeneous porous media approximation is the most common method of representing a fracture network as a continuum. A major assumption of the porous media model is that transport dispersion can be modeled as a Gaussian random process using a dispersivity coefficient to determine the variance of transport about the mean movement. Recently, a number of studies have questioned the validity of the porous media approximation, even for systems that meet the homogeneity requirement (Simmons, 1982; Dagan, 1982; Schwartz et al., 1983).

The discrete approach represents the opposite end of the spectrum. All fractures considered relevant are

modeled as individual entities. The fractures can be described from knowledge of the individual fractures in the system or can be a stochastically generated realization based upon a statistical description of the fracture system. The discrete approach trades the difficulties of determining a representative element for a large amount of information processing. Currently these requirements limit discrete fracture simulations to reservoirs with few relevant fractures or small portions of a fracture system even on large computers. Discrete fracture simulations are a promising approach to determining properties for representative elementary volumes (Dershowitz, 1984; Long, 1985; Schwartz et al., 1983).

At the INEL, a slightly different approach to reservoir scale simulations of fracture systems is under development. The dual permeability approach is a compromise between discrete modeling and continuum modeling. Dual permeability treats the most important fractures in the system discretely and models the rest with representative elements. Despite the similarity of name and function of representative elements and representative elementary volumes these two concepts differ markedly in their characteristics. By incorporating most of the fractures into representative elements, the dual-permeability approach can significantly reduce the processing requirement of the simulation. By treating the most important fractures discretely, the complexity of the representative element is reduced, because the discrete fractures bound the elements providing a well-characterized boundary condition to the element. The complexity of the elements can be controlled by choosing the level of detail modeled discretely. In many cases the dual-permeability approach will allow simulation of reservoirs that are too large for discrete simulation, yet are dominated by a few major fractures or faults, making the continuum representation impossible. The fracture system found at the Raft River geothermal field is an example of a system that is highly dominated by a few large fractures and, therefore, is not readily simulated as continuous media. Figure 2.1 was generated using statistical distributions of fracture spacing based on acoustic televiewer log data from Raft River (Miller et al., 1984).

Figure 2.1 is the motivating example for this analysis. In Figure 2.1, a few large and widely spaced fractures comprise two dominant fracture sets. A third set of small closely spaced fractures completes the flow net. The first observation to be made from Figure 2.1

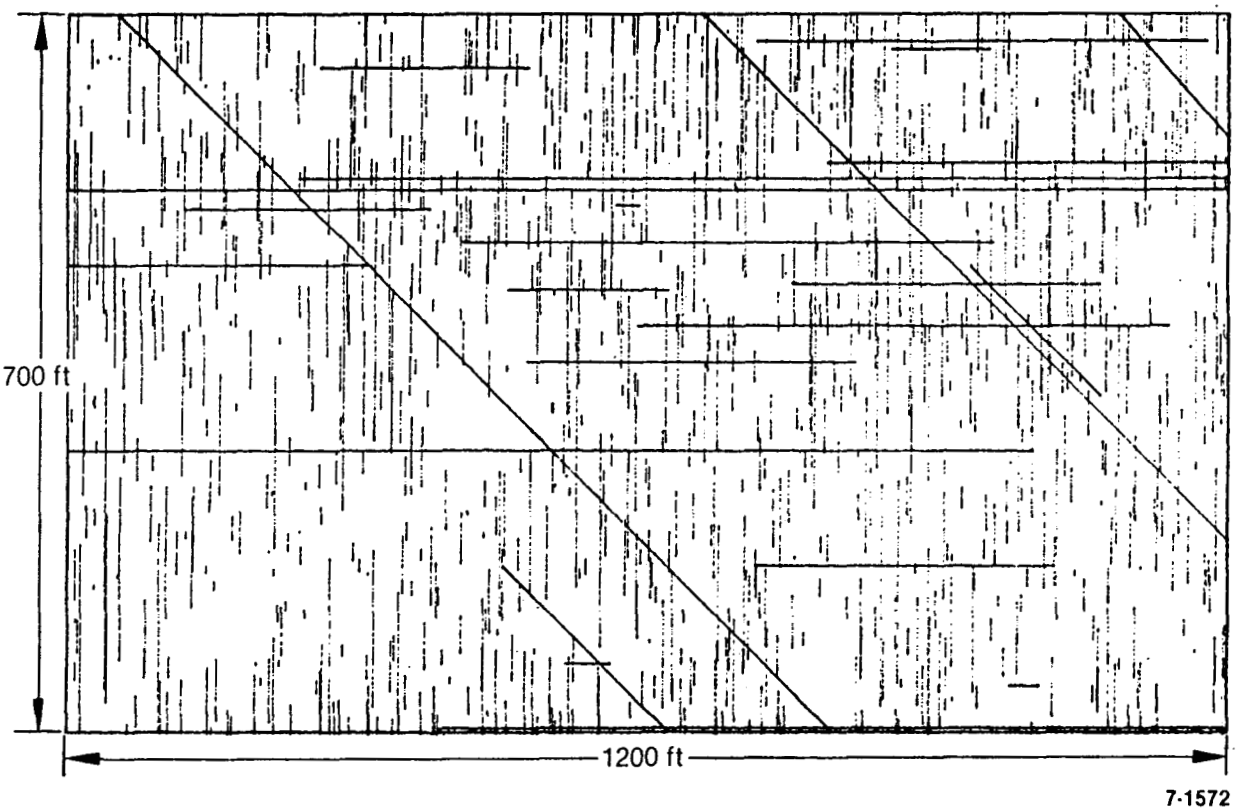

Figure 2.1. Two-dimensional representation of a fracture system. Spacing acquired from Raft River data.

is the relative scarcity of the large fractures. To model this system with a continuum model would require a much larger representative elementary volume than depicted in the figure. The second observation to note is the large number of small fractures. A discrete simulation of this system would have to ignore most of these fractures. Unfortunately, these lesser fractures may provide a significant hydraulic connection between the larger fractures.

The figure provides motivation to develop a two-dimensional representative element for a single set of parallel fractures, the closely spaced set in Figure 2.1. The representative element must simulate the hydraulic connection provided by this set. It must also simulate the transport dispersion characteristics of the fracture set. One option is to develop type curves based on discrete fracture simulations of various realizations of the fracture set. The geometry of a single parallel set of fractures makes stochastic analysis a viable tool to develop the element models.

Before proceeding with the model development, an aside on complexity is needed. This paper deals with the most simple case that can be studied analytically: a single set of parallel fractures. The next level of complexity involves two fracture sets which intersect. If few intersections occur in these sets, then the system is amenable to stochastic analysis. Two fracture sets with frequent intersections are more complex. Whether these systems can be solved analytically or must be developed from dual permeability or discrete simulations is not clear. A system with multiple intersecting fracture sets is probably beyond stochastic analysis. The power of the dual permeability approach will allow these more complex elements to be built up from simpler elements. The following sections treat the simplest geometry, keeping a general approach for application to more complex systems.

2.3 Fracture System Characterization

A statistical description of fracture sets comprising the system is required before a representative element model can be developed. This subsection identifies the parameters that may affect the element properties. A brief review of current statistical models is presented along with the statistical models chosen for this analysis.

Evans (1983) provides an excellent discussion of statistical distributions of fracture parameters. The fracture sets can be described by probability functions of location or spacing, extent or size, fracture aperture, shape, and orientation. Fracture surface characteristics and fracture tortuosity are also important, although these factors are not considered in this development. Fracture shape may be an important factor in developing a representative element. For this treatment however, all fractures are assumed to be of the same depth into the plane of the element.

The spacing between fractures found from line samples have been described as lognormal or exponential (Evans, 1983). Exponential spacing results from a uniform random placement of fractures in space and is assumed for this study. A lognormal distribution would have only a minor impact on the development described below.

The length of fractures is assumed to be distributed as a negative exponential. Lognormal length distribution is also commonly used. The lognormal distribution was investigated but dropped due to the intractability of the resulting equations. Orientation is treated as fixed within the set.

The consequences of different assumptions about aperture characteristics were easily studied. The fracture aperture is assumed variously as (a) constant, (b) lognormal, (c) proportional to length, and (d) lognormally distributed about a mean proportional to length. In the latter assumption, the variance of the logarithm of aperture is constant. A lognormal distribution is believed to result from the multiplicative effects of different distributions (Hahn, 1967). In this light, given a proportionality of mean aperture and length, a constant variance of the logarithm seems the most appropriate assumption for the aperture.

2.4 Element Development

As previously mentioned, a very simple class of representative elements are discussed. Specifically the element is a two-dimensional representation of a single set of parallel fractures. The elements are rectangles such that two sides are in the plane of the fracture faces and the other two sides are normal to the fracture faces (Figure 2.2). The normal sides are treated as constant head boundaries, with the other sides having a no-flow condition.

The representative element considered here must simulate pressure response, bulk flow, and transport. Pressure and flow modeling require both a capacitive term to model the pressure response to fluid storage and a conductive term.

Storage is a bulk property determined for the reservoir as a whole. The storage of an individual element is determined by the reservoir storage multiplying the volume represented by the element.

Hydraulic conductivity and fluid transport require more complex analysis than the storage term. The development of these properties and their dependence on the statistical model assumptions are presented in the next two subsections.

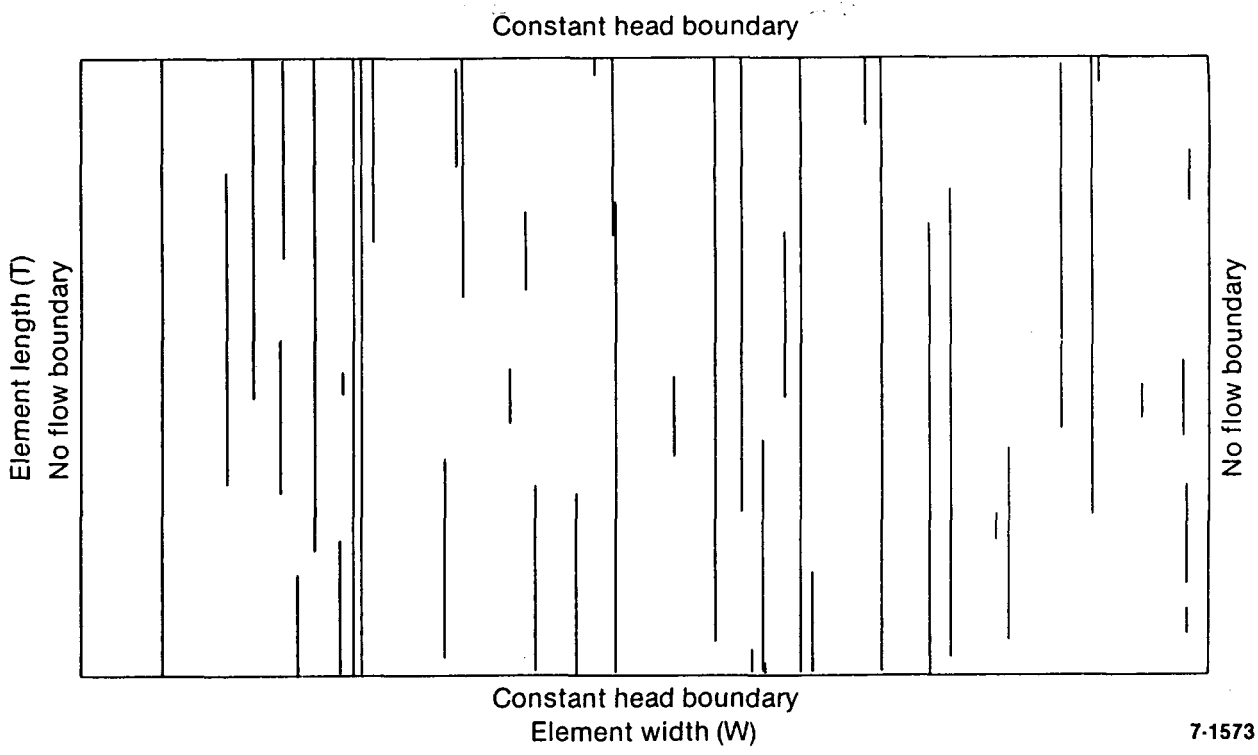

Figure 2.2. Example representative element.

2.5 Hydraulic Conductivity

Conductivity requires a calculation of the average flow through the element for a unit pressure differential. The parallel fracture system requires only a conductivity between the two fixed head boundaries. More complicated elements will require a conductivity tensor in two and three dimensions. All fractures that act as a flow path contribute to the conductivity. Limiting the model to laminar flow, the average velocity along a fracture is related to the pressure drop by (Lamb, 1945)

$$v = \frac{\rho g}{12\mu} b^2 \frac{d\phi}{dx}. \tag{2.1}$$

The flow is then the cross-sectional area of the fracture times the average velocity. For constant depth fractures as is normally assumed in two dimensional models, the flow is proportional to the cube of the fracture aperture as

$$Q = \frac{\rho g}{12\mu} b^3 a \frac{d\phi}{dz}. \tag{2.2}$$

The flow through a fracture connecting both sides of an element of length T is

$$Q = \frac{\rho g}{12\mu} b^3 a \frac{\Delta\phi}{T}. \tag{2.3}$$

The conductivity of the fracture is defined as flow per unit pressure gradient or

$$k = Q \div \frac{\Delta\phi}{T} \doteq \frac{\rho g}{12\mu} b^3 a. \tag{2.4}$$

If the aperture is independent of all other factors and is lognormally distributed, then the expected conductivity of a fracture is

$$\langle k \rangle = \int_0^\infty \frac{\rho g}{12\mu} b^3 a \, P_{ln}(b) \, db \tag{2.5}$$

where; $P_{\ell n}$ (b) refers to the lognormal distribution of b

$$\langle k \rangle = \frac{\rho g}{12\mu} b^{-3} a \exp(9\sigma^2/2) \tag{2.6}$$

Equation (2.6) reveals a strong dependence of the average conductivity upon the variance of the logarithm of aperture.

The length distribution of fractures also affects the element conductivity. Only fractures which connect

both sides of the element contribute to flow in this parallel system. Consider fractures with centers, Z, distributed uniformly along the z axis of the element. The fracture will connect the two sides only if the length, ℓ, is such that:

$$\ell > 2Z \text{ if } Z > T/2$$

or

$$\ell > 2(T-Z) \text{ if } Z < T/2. \quad (2.7)$$

This criteria is symmetric about T/2.

For a negative exponential distribution of fracture length, the distribution function of connecting fractures becomes

$$P(\ell) = \frac{1}{\lambda_z} \frac{(\ell - T)}{\lambda_\ell} \exp(-\ell/\lambda_\ell) \text{ for } \ell > T$$

$$= 0 \text{ for } \ell < T. \quad (2.8)$$

For fractures with aperture unrelated to length and expected fracture spacing, the conductivity of the element is

$$\langle k \rangle = \frac{1}{\lambda_s} \frac{\rho g}{12\mu} b^3 \exp(9\sigma^2/2) \frac{\lambda_\ell}{\lambda_z} \exp(-T/\lambda_\ell). \quad (2.9)$$

The expression for conductivity in Equation (2.9) has the units of a material property (i.e., conductivity per unit area normal to the direction of flow). The conductivity of the element is not a material property. It is a measure of the effective hydraulic conductance of a specific element. Equation (2.9) reveals that the effective conductivity of the element decreases exponentially with separation T due to the exponential length distribution of fractures.

The above assumption that aperture is independent of fracture size is not realistic. The following development assumes that the aperture is a direct function of the length as

$$b = \varepsilon \ell. \quad (2.10)$$

The expected conductivity of an element is

$$\langle k \rangle = \frac{1}{\lambda_s} \frac{\rho g}{12\mu} \int_T^\infty \varepsilon^3 \ell^3 P(\ell) d\ell \quad (2.11)$$

$$\langle k \rangle = \frac{1}{\lambda_2} \frac{\rho g}{12\mu} \varepsilon^3 \frac{\lambda_\ell}{Z}$$

$$[T^3 + 6T^2\lambda_\ell + 18T\lambda_\ell^2 + 24\lambda_\ell^3]$$

$$\exp(-T/\lambda_\ell). \quad (2.12)$$

Figure 2.3 presents a comparison of the sensitivity of conductivity to element length, T, for apertures correlated and uncorrelated to fracture length. Figure 2.3 makes it clear that more attention needs to be given to mean fracture length if apertures are assumed to be uncorrelated with length.

If aperture is related to fracture size by a lognormal distribution where $b = \beta\ell$ and $\sigma^2 =$ constant

$$P(B{:}\ell) = \frac{1}{(2\pi\sigma^2)^{1/2}} \frac{\exp -[\ln(b/\beta\ell)]^2 2\sigma^2}{b} \quad (2.13)$$

now

$$\langle k \rangle = \frac{1}{\lambda_s} \frac{\rho g}{12\mu} \int_T^\infty b^3 P(b{:}\ell) P(\ell) db\, d\ell \quad (2.14)$$

which is identical to the direct proportionality case with $\varepsilon = \beta^3 \exp(\sigma^2/2)$.

The conductivities developed above are the expected values for elements of width W. It is important to consider the effect of the width of the element on the variance of the conductivity. The variance of the conductivity of the fractures increases proportionately to the expected number of fractures, W/λ_s contained by the element. The variance in the number of fractures represented by the element is also W/λ_s for an exponential spacing of fractures (Parzen, 1962). These variances of the element conductivity are independent and therefore additive. The conductivity of the elements also increases linearly with W/λ_s which means the relative variance deceases linearly with the element width.

As mentioned earlier, the conductivity determined in this analysis has the units of a material property but is a measure of the expected conductivity of a specific geometry. The representative element properties are strictly modeling tools and should not be construed as a measure of physical properties. This is a major difference between representative elements and representative elementary volumes.

2.6 Transport

Once fluid enters a fracture in this system, it remains in the fracture until it reaches the end of the element. Consider a pulse of solute entering the element at time zero. Following the development presented by Simmons (1982), the distribution of the expected concentration as a function of time and the distance along the element is:

$$c(Z,t) = \int_0^\infty \delta(t - Z/v) P(v) dv = P(Z/t) \quad (2.15)$$

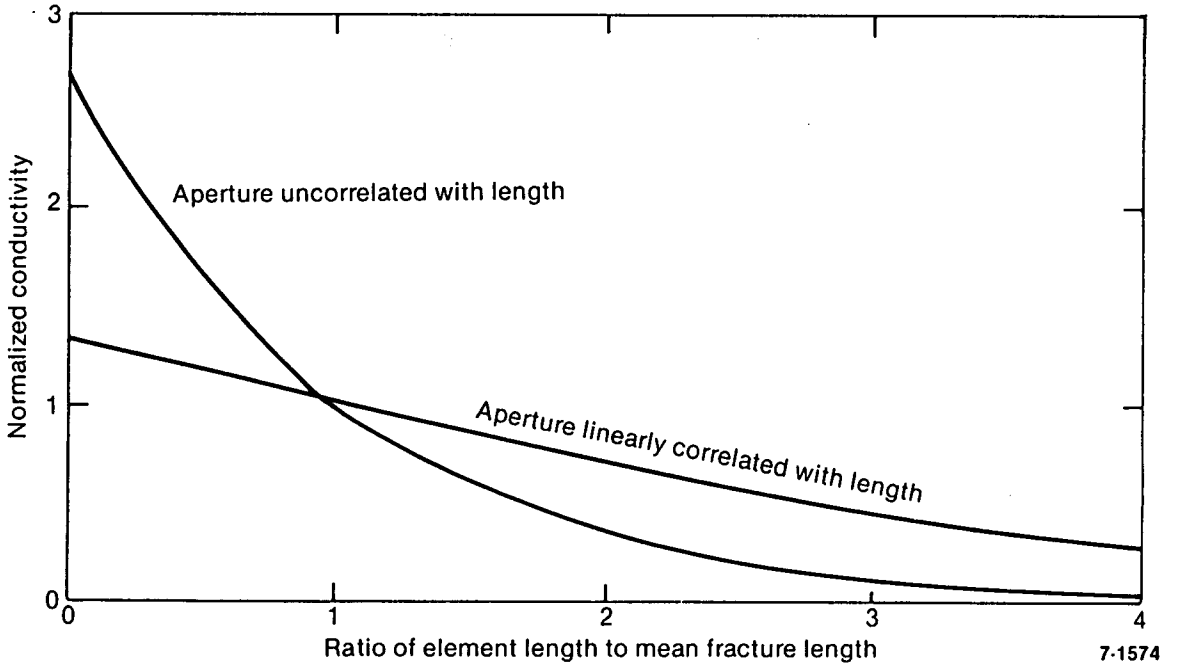

Figure 2.3. Sensitivity of conductance to element length.

The distribution (dispersion) of the pulse is simply a scaled version of the velocity profile. To model the element, the time distribution of breakthrough is needed. Replacing Z by T

$$c(T,t) = P(T/t) \tag{2.16}$$

Based on Equations (2.1) and (2.3)

$$T/t = \frac{\rho g}{12\mu} b^2 \frac{\Delta\gamma}{T} \tag{2.17}$$

$$t = \left(\frac{\rho g}{12\mu}\right)^{-1} \left(\frac{\Delta\phi}{T^2}\right)^{-1} b^{-2}. \tag{2.18}$$

The transit time t is, therefore, directly related to aperture and

$$P(t)dt = P(b)db \tag{2.19}$$

From 18,

$$db = 1/2 \left(\frac{\rho g}{12\mu}\right)^{-1/2} \left(\frac{\Delta\gamma}{T^2}\right)^{-1/2} t^{-1/2}\, dt. \tag{2.20}$$

Given a lognormal aperture distribution as in the first of the three conductivity calculations 2.6, 2.9, 2.12.

$$P(t) = \frac{1}{(2\pi\sigma_t^2)^{1/2}} \frac{\exp - [\ln(t/\bar{t})/2\sigma_t]^2}{t} \tag{2.21}$$

where

$$\bar{t} = \frac{\rho g}{12\mu} \frac{\Delta\gamma}{T^2} b^2 \text{ and } \sigma_t^2 = 4\sigma^2. \tag{2.22}$$

The transit time for a solute packet can be found using the Monte Carlo technique. The effect of the Poiseuille profiles can be incorporated into a Monte Carlo simulation by dividing the transit time by a generated velocity ratio from the Poiseuille velocity distribution. The distribution function is

$$P(\gamma) = 1/3 \left(\frac{\gamma}{1 - 2\gamma/3}\right). \tag{2.23}$$

Where γ is the ratio of the velocity at a random position in the fracture to the mean velocity.

Equations (2.24) and (2.25) present the distribution function for transport given a linear correlation of aperture and fracture length.

$$P(t) = \frac{[1 - (T\gamma/\pi t^{1/2})]}{2\varepsilon^2\lambda_\ell^2}$$

$$\exp - (\kappa) \exp - (t^{1/2}/\gamma\lambda_\ell) \tag{2.24}$$

where

$$\kappa = \left[\frac{\rho g}{12\mu} \frac{\Delta\phi}{T^2} \right]^{1/2} . \quad (2.25)$$

When aperture is lognormally distributed about a fracture length dependent mean, Equation (2.26) defines the probability distribution of velocities. Equation (2.26) does not yield a closed form solution and must be evaluated numerically.

$$P(b) = \int_T^\infty P(b:\ell) P(\ell)\, d\ell \quad (2.26)$$

2.7 Conclusions

The dual permeability approach to reservoir scale simulation has some important advantages over discrete fracture simulation or the continuum approach. These advantages are embodied in the ability to adjust the degree of complication treated discretely versus the complexity of the representative elements. Further, some reservoirs may be simulated by only a dual permeability model.

The dual permeability approach will provide a more robust simulation capacity because the technique does not require homogeneity of the elements. It will allow the modeler to treat highly important fractures discretely and yet retain full information of the influence of the minor fractures.

The primary research needed to develop dual permeability modeling is the development of representative elements. This study involved the simplest of fracture systems to be modeled as a representative element. The study provided a complete description of the hydraulics and transport properties of this class of two-dimensional elements. These elements can be used in a dual permeability model, which simulates transport of solute as discrete particles.

Even these simple elements can provide a significant reduction in simulation cost. More complicated elements can also be created, although some tough problems need to be addressed. The first hurdle is the description of a fracture intersection, both hydraulically and in terms of transport. Fracture intersections will introduce transition probabilities into the transport equation. Once the simple elements have been described, more complicated elements may be amenable to analytic development. If not, a dual permeability model can be used to empirically find the element properties as is now done to develop continuum models.

2.8 Bibliography

Dagan, G., "Stochastic Modeling of Groundwater Flow by Unconditional and Conditional Probabilities," *Water Resources Research*, 18, 4, 1982, pp. 835-848.

Dershowitz, W. S., *Rock Joint Systems*, Ph.D. thesis, MIT, 1984. Evans, D. D., Unsaturated Flow and Transport Through Fractured Rock Related to High-Level Waste Repositories, NUREG/CR-3206, University of Arizona, 1983, pp. 34-43.

Hahn, J. P., *Statistical Models in Engineering*, Wiley, 1967.

Lamb, H., *Hydrodynamics*, New York: Dover, 1945.

Long, J. C. S., *Verification and Characterization of Continuum Behavior of Fractured Rock at AECL Underground Research Laboratory*, BMI/OCRD-17, LBL-14975, University of California, February 1984.

Miller, J. D., D. W. Allman, D. Wulf, *Raft River Fracture Characterization and Reservoir Simulation*, SE-PB-84-58, Idaho National Engineering Laboratory, 1984.

Parzen E., *Stochastic Processes*, Holden-Day, 1962.

Schwartz, F. W., L. Smith, A. S. Crowe, "A Stochastic Analysis of Macroscopic Dispersion in Fractured Media," *Water Resources Research, 19*, 5, 1983, pp. 1253-1265.

Simmons, C. S., "A Stochastic-Convective Transport Representation of Dispersion in One-Dimensional Porous Media Systems," *Water Resources Research, 18*, 4, 1982, pp. 1193-1214.

3. DUAL PERMEABILITY MODELING OF FLOW IN A FRACTURED GEOTHERMAL RESERVOIR

John D. Miller and David W. Allman
Idaho National Engineering Laboratory

A three-dimensional fracture system synthesis and flow simulation has been developed to correlate drawdown characteristics measured in a geothermal well and to provide the basis for an analysis of tracer tests. The study is an extension of the dual permeability approach in which discrete and distributed fracture flows are incorporated in a common model to better represent a fractured media within computer limitations. Simulations are conducted on multiple scales where each smaller simulation (or core testing) determines the distributed properties for the next larger simulation. A fracture system was synthesized from acoustic televiewer data on the orientation and separation of three distinct fracture sets together with additional data from the literature. Lognormal and exponential distributions of fracture spacing and radius were studied, with the exponential distribution providing more reasonable results. Hydraulic apertures were estimated as a function of distance from the model boundary to a constant head boundary. Mean apertures of 5.7, 101, and 16 μm were chosen as the most representative values for the three fracture sets. Advances in fracture characterization which may ultimately reduce the uncertainties in this type of model are discussed.

3.1 Introduction

The objective of the work presented is to model the flow system in the vicinity of a geothermal well as the basis for a subsequent correlation of measured tracer responses. Data from Raft River Well RRGP-5B were used as the basis for the study. This well was tested from September through November 1982 as part of a DOE research program on the injection of spent geothermal fluids. A series of drawdown tests were conducted along with a number of injection-backflow tracer tests. This analysis is part of an ongoing effort incorporating field studies and analytic, physical model, and computer simulations. This effort is directed toward an understanding of the processes controlling the movement of fluids in a geothermal reservoir. The following subsections provide a summary of the modeling approach and its computer implementation, the RRGP-5B borehole fracture characterization, the fracture system synthesis and flow correlation, and recent advances in fracture characterization.

3.2 Modeling Approach

Transport in fractured media occurs in three distinctly different geologic structures: faults, macrofractures, and microstructures. Faults or fault zones constitute the longest and highest permeability paths and are assumed to be located during drilling or geophysical borehole logging.

Macrofractures occur over a continuous spectrum of size ranging from centimeters to many meters. They are largely extensional and are probably partially mineralized. Their geometric properties are determined as probability density functions by core sampling or borehole logging. Limited hydraulic and transport characterization may be performed by packer testing. Flow occurs in these fractures down to a limiting aperture of 0.2 μm (Romm, 1966) with diffusion persisting below this level.

The microstructure encompasses all connected passages at the grain scale, including pores and intergranular and intragranular cracks. Probability density distributions of geometric properties would be substantially different from those of the macrofractures but, as subsequently discussed, are not required.

Each of these structures is included in the model developed in this report. The approach is an extension of earlier work on two-dimensional models by Miller (1983), Clemo (1985) and Hull (1985). The analytic basis for the approach is given by Clemo (1986). In this approach, the faults are treated as deterministic constant head boundaries, which may be remotely located from the boundary of the detailed model area. The microstructure is treated as a continuum at the scale of the core sample. Its properties are determined by specific flow and transport testing of that core.

It is the treatment of the macrofractures which is unique in the dual permeability approach. In this approach, the larger fractures are treated discretely and the smaller ones are distributed throughout the region. The dual-permeability feature is incorporated in multiple models of differing scale, with each of the smaller models (or core testing) providing distributed or representative element properties to the next larger scale model. The advantage of this approach is that each model incorporates a limited number of discrete

fractures, consistent with computer limitations, while representatives of all sizes are included.

The models, of necessity, incorporate a number of approximations. As is common in current discrete fracture analysis and simulation, fractures are idealized as parallel-sided, planar, circular discs. Real fractures are rough, curved, or laterally stepped and are probably not circular due to interference with other fractures. Indeed, some fractures terminate on other fractures (Dershowitz et al., 1985). A review of work on the geometry of single real fractures and the modeling of flow and transport in these fractures is given by Miller et al. (1986).

The model includes three differently oriented fracture sets and neglects the variation of fracture orientation from the mean of each set. It also includes a hydrofracture created during development of the well. The treatment of the intersections of the fractures in the different sets introduces another set of approximations. Figure 3.1 shows the approach given by Huang and Evans (1985) and adopted for this study: a given fracture intersects another fracture (or the boundary of the model) in a line. The head is assumed constant over the length of the line and is located, for reference, at a node at the midpoint of the line. A flow path exists in a fracture between two lines of intersection. Laminar flow is computed in this path using the cubic law (Lamb, 1945) in which flow varies as the cube of the aperture. The length of the path is the distance between nodes, and the width is approximated as the average of the two intersection lengths, without consideration of their orientation. As shown in Figure 3.1, in a fracture with more than two intersections or nodes, flow is computed independently between each node and every other node. Rasmussen (1986) has extended the Huang and Evans approach to include a boundary element solution for the actual flow distribution between two or more fracture intersections. His solution incorporates a no-flow condition at the fracture edge. The addition of this or some other sophistication to the dual permeability model is deferred to future studies.

The analysis departs from the Huang and Evans approach in the inclusion of the distributed fracture flow paths. As described previously, the conductivities of these paths are determined from representative element simulations with the larger fractures excluded. Separate representative element simulations are conducted to determine the conductivity normal to each of the synthesized fracture sets or the hydrofracture.

Figure 3.2 shows the computational process. Consider a fracture (upper left) somewhat smaller than those addressed discretely in a particular model, which bridges two discrete fractures of a common set. The contribution of this fracture to the conductivity between the two large fractures is computed discretely and is averaged, in the representative element at the lower left, over the cross-sectional area of that model. Applying the resultant conductivity over the shadow or overlap area between the two discrete fractures in the larger-scale simulation (lower right) then introduces the requirement that the distributed fracture lies in a region which intercepts both global fractures. The resulting distributed flow is shown in Figure 3.2 at the upper right. The discrete pathway due to the small fracture has been replaced by the conditions that a fracture be long enough to bridge the gap and that it occurs in a suitable lateral position.

This model incorporates the simplification that distributed flow may only occur between (parallel)

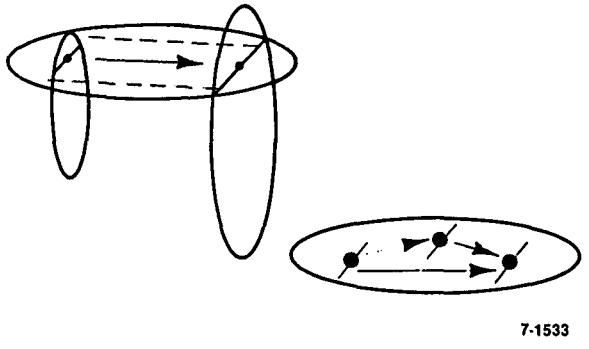

Figure 3.1. Discrete fracture flow paths.

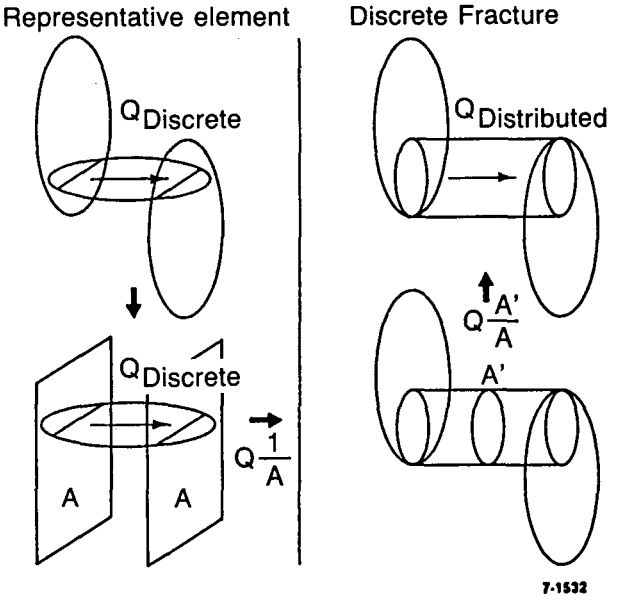

Figure 3.2. Distributed fracture flow paths.

fractures of the same set. This is based on the notion that an adjacent fracture of a different set would probably communicate with the reference fracture by direct intersection. A more complex calculation is considered desirable for future studies.

The determination of the distributed fracture paths to the hydrofracture in RRGP-5B is more complex, since the hydrofracture is not parallel to any of the fracture sets. A probabilistic fracture is assigned a distributed fracture path to the hydrofracture if it shadows it without shadowing a fracture nearer to the hydrofracture. These calculations are made neglecting the angle between the fractures and the hydrofracture. The path cross section is the area of the entire fracture as projected onto the plane of the hydrofracture and its length and conductivity are computed as before.

In all cases, distributed fracture flow is computed using the average heads for each of the two fractures. It should be noted that this calculation identifies the entire fracture as a pressurized body that receives or provides flow to the smaller fractures that intercept it.

The thickness of the representative element model is an important parameter. As shown by Clemo (1986), the conductivity between two planes decreases with increasing separation between those planes because of the reduction in number of cross fractures large enough to directly span the separation. Thicknesses were chosen equal to the mean separation of the corresponding fracture set, or the mean distance to the hydrofracture, in the larger model.

Figure 3.3 summarizes the essential features of the approach, as applied in this study. The global model at the top of the figure is the largest scale studied. It incorporates:

- Discrete flow paths in the planes of the large fractures due to their intersections with other fractures
- Distributed flow paths between fractures of the same set with conductivity determined from the representative element model as the distributed effect of the smaller fractures
- Connections from the fracture-boundary intersections to remote constant head boundaries
- A flow boundary representing the well.

The representative element models at the bottom of the figure are oriented to determine the conductivity normal to each of the fracture sets. Each has its thickness equal to the mean separation of the fractures in its normal set in the global model. All of these models include fractures of a common size range, which is smaller than that included in the global model. The effect of still smaller fractures is incorporated in the distributed flow paths.

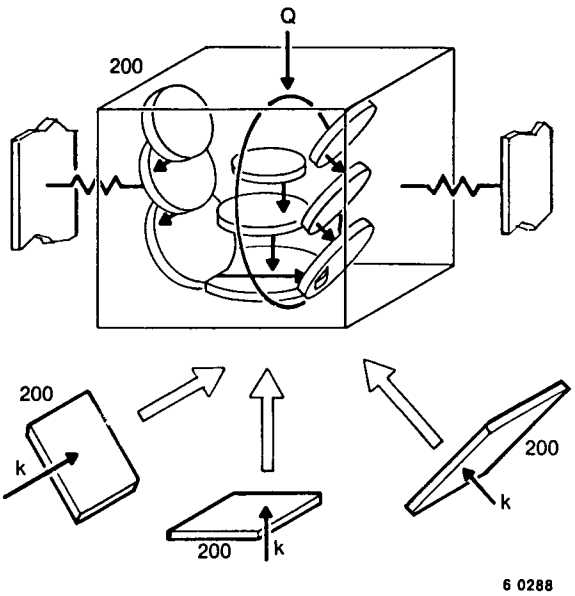

Figure 3.3. RRGP-5B model.

The model reported in this study is limited to a two-level flow simulation. In addition, the distributed paths within the smaller scale model have only a slight contribution to the overall flow system and have been neglected. Complete multiple level simulation would, however, be required for transport modeling because the preponderance of rock surface and the importance of diffusion in the smaller passages.

3.3 Computer Implementation

The global and distributed element models described above are each implemented in a sequence of two codes which are together called FRACSL3D (FRactured media flow and transport - Advanced Continuous Simulation Language, 3D). The first code is initiated with a synthesis of fracture location, orientation, and radius. The fracture-to-fracture and fracture-to-boundary intersections were then found using subroutines developed by Huang and Evans (1985). In the case of the global model, the hydrofracture and distributed flow paths are also included. Information about the fracture, distributed fracture path, and intersection information was then output to a data file.

The second code reads the data file and any additional data, calculates the fracture paths, and solves for the head and flow distributions. This program was developed at the INEL as a series of subroutines with supporting routines from the ACSL (Advanced Continuous Simulation Language) problem solver code (Mitchell and Gauthier, 1986). Apertures, widths, lengths, and conductivities are computed for the

various fracture paths. Boundary conditions are then applied. A first-order differential equation is written for the conservation of mass at each node, and the steady-state flow and head distribution is found by iterating to drive the head derivatives to zero.

Both codes are implemented on a CDC CYBER 176 computer with 130,368 decimal words of small core available to the user. The flow code is limited to 160 nodes, while the synthesis code can analyze much larger systems. Work is in progress to expand the capability of the flow code.

3.4 Raft River Well RRGP-5B Borehole Fracture Characterization

Raft River Well RRGP-5B was completed in quartzite and schist at a depth of 4911 ft. An acoustic televiewer survey was made by the U.S. Geological Survey over a 495-ft borehole interval prior to well completion. A second survey of the production interval, made after the production liner was installed and the well was hydrofractured, showed no new fractures other than the hydrofracture itself. A total of 142 discontinuities were found in the 495-ft precompletion survey. Figure 3.4 shows a plot of borehole spacing vs. cumulative frequency of occurrence for the region between 4445 and 4695 ft. This region was selected because it includes the observed portion of the hydrofracture below the liner and the postulated portion above the bottom of the liner. The data for three distinct fracture sets are fitted by lognormal distributions. Table 3.1 summarizes the characteristics of the three fracture sets.

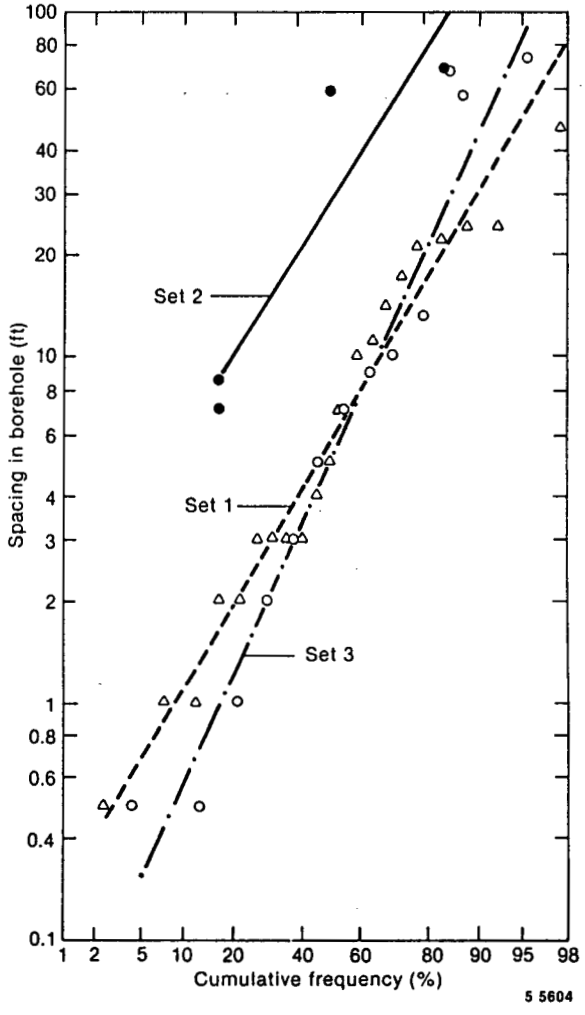

Figure 3.4. Fracture spacing.

Table 3.1. Well RRGP-5B fracture set characteristics—depths 4445 to 4695 ft

Set	Number of Separations	Strike	Dip	Mean of Log_{10} of Borehole Spacing (ft)	Standard Deviation of Log_{10} of Borehole Spacing (ft)	Mean Normal[a] Spacing (ft)
1	21	N12W	79E	0.753	0.539	2.036
2	3	N34E	46E	1.480	0.551	30.77
3	12	N18W	20E	0.701	0.708	14.17

a. Normal spacing = (borehole spacing) (cos dip).

3.5 Fracture System Synthesis

As shown schematically at the top of Figure 3.3, the global model is established by describing the well, the hydrofracture, a model space, and the probabilistic fractures within that space. Based on acoustic televiewer observations of the portion of the wellbore below the well liner, the hydrofracture was described as a 100-ft radius circle, centered on the bottom of the liner and oriented in a vertical plane with strike to the north. A cubic model space 200 ft on a side was chosen to surround the hydrofracture and thereby model the distribution of flow from the well through the hydrofracture and into the formation. This volume was centered on the bottom of the wellbore liner and oriented with vertical faces running North-South and East-West.

In the initial synthesis of probabilistic fractures, the spacing between successive members of the same set was based on the lognormal distribution shown in Figure 3.4 and Table 3.1. Since this distribution is that of a scanline (borehole) sampling, the spacing between fractures, which are located laterally throughout the complete model region, must be considerably smaller. The model separations were adjusted until scanline samplings equaled the measured mean separations.

These results are sensitive to the fracture radius distribution. Radius distributions are not known for the Raft River fracture system, so data on radius-to-spacing ratio from the literature were used. Mahtab et al. (1973) reported trace length, separation and physical apertures for a copper mine in a batholith. Three nearly orthogonal fracture sets were found in quartz monzonite and in monzonite porphyry. While the distributions were not fitted by the author, the means were given. The mean trace lengths reported by Mahtab et al. were first multiplied by 0.635 to provide the expected value of radius. The ratio of mean-radius-to-mean-spacing, averaged over the six fracture set-rock type combinations, was found to be 3.15. Gale et al. (1985) reported mean-radius-to-mean-separation values for the Stripa ventilation drift which average 1.15 for the four fracture sets. A value of 2.15 was assumed for the Raft River analysis as the mean of the values from the literature. The distribution for the first analysis was assumed to be lognormal.

Fractures were synthesized within a 300-ft cube, centered on and parallel to the model cube. The additional space was provided to extend fractures into the model from centers located outside the model. Synthesis and scanline studies were conducted separately for each of the three fracture sets.

In order to reduce the number of nodes to the capability of the flow code, it was necessary to limit the discrete fractures in this model to those larger than 250-ft radius. Two observations can be made from this result. First, the resulting model is unsatisfactory since the extra fracture generating space outside the model only provides for fractures with radii less than 50 ft. The second, and the more significant observation, is the synthesized fracture system is dominated, probably excessively so, by large fractures. Reduction of the mean-radius-to-mean-spacing ratio of 2.15 would probably not affect the results significantly, since a larger number of fractures would then be required to match the observed scanline spacing.

The acoustic televiewer spacing data are obviously well-fitted by the lognormal characteristic shown in Figure 3.4, but it should be noted that the smaller fractures may not have been detected. In the literature as reviewed by Evans (1983), scanline length distributions were best fitted by a lognormal distribution by some researchers, while an exponential distribution provided the best fit to data for others. In addition, a power law distribution with frequency varying with trace length to an exponent between -1.3 and -1.8 was found best by Segall and Pollard (1983). The analysis of fracture permeability at the Stripa ventilation drift by Gale et al. (1985) utilized both lognormal and exponential distributions.

As an alternative, a second analysis was performed for exponential distributions of spacing and radius, again differing by a factor of 2.15. The exponential spacing was provided by randomly locating the fracture centers in the normal direction (Priest and Hudson, 1981). The single parameter in the exponential distribution of the spacing, the mean value, was chosen as the arithmetic mean of the measured spacings. Fractures were located randomly in the three directions until a scanline accumulated the number of interceptions which provided the required mean spacing. This procedure was modified analytically to avoid treating the very large number of small fractures which would not intercept the scanline. The distribution of radii was limited to the larger values and the mean spacing for the scanline was increased accordingly. After providing for the correct scanline sampling rate, the fractures simulated discretely in the global analysis were limited to those greater than 100-ft radius to restrict the number of fracture-fracture and fracture-boundary intersections to 160. The smaller fractures were used in individual representative element models to evaluate the conductivity normal to the hydrofracture and fracture sets 2 and 3. Distributed flow between global fractures in set 1 was neglected, since these fractures are widely separated. Fracture radii in the representative elements were limited to a maximum of 100 ft and minimums of 11 to 15 ft. Table 3.2 summarizes the four geometric models.

Table 3.2. Global and representative element models—exponential distribution of spacing and radius

Model	Fracture Generating Region[a] (ft)	Model Region[a,b] (ft)	Fracture Radius (ft)	Fractures (No.)	Internal Nodes (No.)	Boundary Nodes (No.)	Discrete Fracture Paths (No.)	Distributed Fracture Paths (No.)	Representative Element Conductivity[c] (ft/day)
Global	600/600/600	200/200/200	above 100	31	64	102	765	14	—
Element 1[d]	400/250/400	200/50/200	32 to 100	33	32	114	294	—	0.0472
Element 2	238/400/400	38/200/200	27 to 100	23	20	98	131	—	0.0209
Element 3	239/400/400	39/200/200	27 to 100	26	41	98	310	—	0.2520

a. x by y by z.

b. Model region centered in fracture generating region.

c. Representative element for conductivity nomal to hydrofracture.

d. Through smallest model dimension; at aperture-to-radius ratio = 0.5E-5.

3.6 Flow Correlation

Drawdown tests were conducted at Well RRGP-5B at flow rates ranging from 75 to 300 gpm. Steady-state conditions were reached in an average of 235 s after the start of drawdown and the well recovered to the initial condition in an average of 130 s after the end of production. Figure 3.5 shows the variation of drawdown flow rate and recovery at steady-state. The drawdown and recovery heads are essentially identical and the mean values rise with increasing flow at a rate greater than linear. The formation flow characteristics, found by subtracting a calculated wellbore loss, also rise at a greater than linear rate, showing the presence of nonlinear or turbulent flow in the formation. However, nonlinear flow cannot be accommodated in the present model because of the treatment of multiple independent flow paths, as stated in Section 3.2. The analysis was completed by performing a linear analysis and then determining its validity on the basis of roughness and Reynolds numbers. A linear formation drawdown was estimated by drawing a tangent to the initial portion of the formation drawdown curve.

Predicted linear drawdowns were found by solving for the flow distributions in the four geometric models previously described. Flow solutions for the three representative element models yielded conductivities for a particular aperture-to-radius value. These conductivities were then incorporated in the global model where a single value of aperture-to-radius ratio was used to adjust the apertures and the conductivity of both representative element fractures and global fractures. The selection of a distance from the model boundary to a remote, fixed-head boundary completes the input set and a flow solution is obtained. Since all component head rises are dependent on the cube of the aperture, system head rises for other values of aperture-to-radius ratio are obtained by a simple ratio.

The contribution of the representative elements to the computed drawdown was found by zeroing the representative element conductivities used in the global flow simulation and solving for the modified head distribution. The drawdown increased by 9.0%, corresponding to the cube of the ratio of the dominant apertures in the representative element models to those in the global model.

The validity of the solution with reference to the observed nonlinear flow was then examined. As summarized by Gale et al. (1985), the onset of nonlinear flow has been observed at a Reynolds number of 80 at a relative roughness of 1.0 and at about 100 at a relative roughness of 0.862. The average Reynolds number over the 534 discrete fracture paths in the global model is 10.5, based on a hydraulic diameter equal to twice the aperture. This value is independent

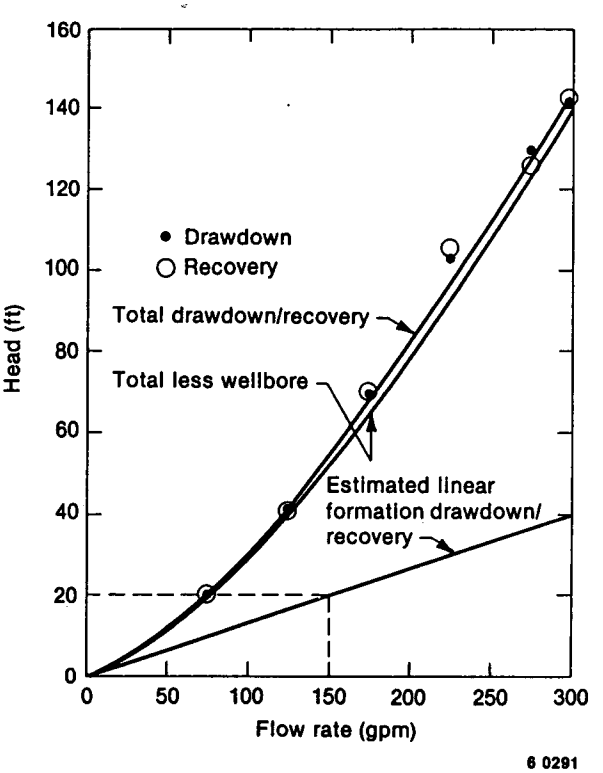

Figure 3.5. Measured and linear drawdown characteristics.

of the aperture values for a system otherwise fixed in flow and geometry. True Reynolds numbers, however, range to considerably higher values because the model has multiple fracture paths in a given portion of a fracture. Indeed, 120 fracture paths occur in the largest fracture in the system (273-ft radius) and 66 fracture paths occur in the 100-ft radius hydrofracture. Since these tend to be the longest paths in the system, a substantial portion of the flow path may have effective Reynolds numbers greater than 100. In the absence of information on fracture roughness, the analysis was completed by matching values predicted by linear flow relationships to the estimated linear formation drawdown shown in Figure 3.5.

Figure 3.6 shows the variation of predicted drawdown with remote boundary distance and aperture-to-radius ratio for a 150-gpm flow rate. A 100-ft distance was chosen as the best estimate, based partially on the detection, during drilling, of a high transmissivity aquifer at a point near the top of the modeled region. While this does not define the distances to a constant head boundary from the other five faces of the model, the previously discussed 235-s (drawdown) and 130-s (recovery) times tend to confirm the existence of relatively close constant-head boundaries. The mean set apertures at the 100-ft remote boundary distance and a 20-ft linear drawdown are 6.7, 101, and 46 μm

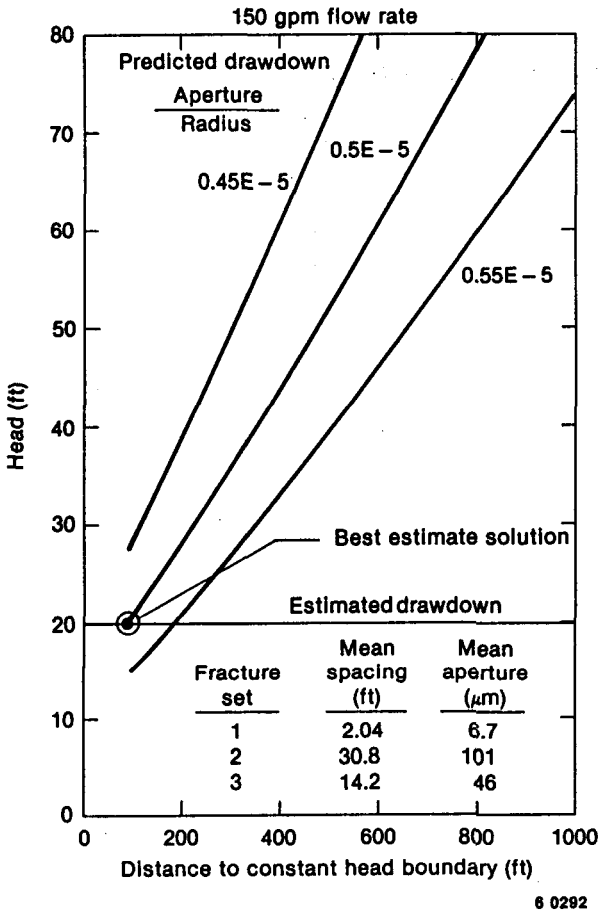

Figure 3.6. Linear drawdown correlation.

for sets 1, 2, and 3, respectively. These values are subject to considerable uncertainty regarding the shape of the spacing and radius distributions, as well as the mean of the radius distribution and the nonlinear flow term. Consequently, these values may only be accurate to within a factor of three. They may be compared to hydraulic apertures of 6 μm at Stripa, Sweden (Gale et al., 1985) and 11.8 μm at Chalk River, Canada (Raven et al., 1985). In addition to the difference in natural fracture systems, it should be noted that the Raft River fractures may have been opened by the hydraulic stimulation treatment.

Work is in progress to streamline the codes and to refine the analysis to include multiple realizations of the global and representative element fracture systems.

3.7 Advances in Fracture Characterization

A substantial body of work on fracture mapping and characterization has been reported since well RRGP-SB was completed and tested. Most of this work has been sponsored by the programs for deep geologic storage of high-level radioactive waste. Acoustic televiewer data have been complemented by the use of the tube wave device (Paillet and Keys, 1984), which shows the presence of water in a fracture intersecting the wellbore as a discontinuity in an acoustic wave propagated down the borehole. The same authors discuss the use of the heat-pulse flow meter, which measures extremely low velocities in the wellbore as a means of detecting fluid bearing fractures. The microelectrical scanner tool (MST) creates an electrical image from an array of sensors pressed against the wellbore and is capable of imaging open fractures with lengths less than 10 cm and widths less than 1 mm (Plumb et al., 1985). Neutron logging correlated well with conductivity measurements at the Oracle test site in Arizona (Jones et al., 1985), and additional fracture characterization was provided by oriented cores. Doe and Osnes (1985) present methods for determining fracture characteristics from packer testing of individual fractures. The use of multiple borehole terminations would provide data on fracture persistence, which could help define fracture radii. The extent of a fracture, and the flow resistance and dispersion in that fracture, may ultimately be defined on the basis of a detailed description of its aperture distribution derived from core samples and generic correlations (Miller et al., 1986). Another approach which may help determine fracture characteristics is the application of existing technology to the description of the structural and hydrothermal processes that created the fracture system. Approaches such as those by Segall and Pollard (1983) and Knapp and Norton (1981) may be developed to correlate borehole characterization data and, in so doing, provide a quantitative description of fracture characteristics not easily obtained from borehole studies.

The development of these techniques is being supported by the geologic repository programs. However, a field program which integrates capabilities in instrumentation, testing, evaluation and modeling is in order to provide an assessment of specific costs and benefits in a geothermal application.

3.8 Summary

A dual permeability simulation of fracture system flow has been developed as an effective means of simulating the range of fracture size in a three dimensional discrete fracture model within the limitations of computer cost and core size. A global model incorporates discrete representations of the larger fractures and a distributed or representative element representation of the smaller fractures. The conductivity of the representative element is found by a separate discrete

simulation of the smaller fractures or by core testing. The combined simulation incorporated fractures with radii as small as about 15% of the dimension of the model. The level of detail and the cost of the simulation are such as to permit, with suitable model extensions, accurate studies of solute transport in fractured geothermal systems.

Definition of the fracture system in this study depended on the form of the distribution of spacing in three-dimensional space and on assumptions about fracture size distribution. In addition, smaller uncertainties were introduced by the absence of a defined pressure boundary condition and by the presence of nonlinear fracture flow. Further information on fracture characteristics could be provided by the addition of a transport model and correlation with measured tracer responses. The uncertainties in these studies can be reduced by more extensive fracture characterization data obtained on the basis of recent advances in flow measurement, tube wave, microelectrical and neutron logging, and from oriented cores. Further data may ultimately be provided by methods involving packer testing, characterization of aperture variation over a single fracture, and correlating sampled data with a structural-hydrothermal rationale for the evolution of the fracture system.

3.9 Bibliography

Clemo, T. M. , "FRACSL Code Development and Correlation of East Mesa Test Results," *Proceedings, 10th Workshop on Geothermal Reservoir Engineering, Stanford University*, January 1985, pp. 287-292.

Clemo, T. M., "Representative Element Modeling of Fracture Systems Based on Stochastic Analysis," *Geothermal Injection Technology Program, Annual Progress Report, FY-86*, 1986.

Dershowitz, W. S., B. M. Gordon, J. C. Kafritsas, "A New Three-Dimensional Model for Flow in Fractured Rock," *Proceedings International Association of Hydrogeologists Symposium on Hydrogeology of Rocks of Low Permeability, Tucson, January 1985*, pp. 441-448.

Doe, T. W. and J. D. Osnes, "Interpretation of Fracture Geometry from Well Tests," *Proceedings, International Symposium on Fundamentals of Rock Joints, Bjorkliden, Sweden, September 15-20, 1985.*

Evans, D. D., *Unsaturated Flow and Transport Through Fractured Rock - Related to High-Level Waste Repositories*, NUREG/CR-3206, March 1983.

Gale, J. E., A. Rouleau, L. C. Atkinson, "Hydraulic Properties of Fractures," *Proceedings International Association of Hydrogeologists Symposium on Hydrogeology of Rocks of Low Permeability, Tucson, January 1985*, pp. 1-16.

Huang, C. and D. D. Evans, *A 3-Dimensional Computer Model to Simulate Fluid Flow and Contaminant Transport Through a Rock Fracture System*, NUREG/CR-4042, January 1985.

Hull, L. C., "Laboratory Validation of a Dual-Permeability Reservoir Code," *Proceedings, Tenth Workshop on Geothermal Reservoir Engineering, Stanford University, January 1985*, pp. 293-296.

Jones, J. W., et al., *Field and Theoretical Investigations of Fractured Crystalline Rock Near Oracle, Arizona*, NUREG/CR-3736, August 1985.

Knapp, R. B. and D. Norton, "Preliminary Numerical Analysis of Processes Related to Magma Crystallization and Stress Evolution in Cooling Pluton Environments," *American Journal of Science, 281*, January 1981, pp. 35-68.

Lamb, H., *Hydrodynamics*, New York: Dover Publications, 1945.

Mahtab, M. A., D. D. Bolstad, F. S. Kendorski, *Analysis of the Geometry of Fractures in San Manuel Copper Mine, Arizona*, Bureau of Mines RI 7715, January 1973.

Miller, J. D., "A Fundamental Approach to the Simulation of Flow and Dispersion in Fractured Media," *Proceedings, 9th Workshop on Geothermal Reservoir Engineering, Stanford University*, December 1983, pp. 373-379.

Miller, J., L. C. Hull, R. P. Smith, *Fracture Flow Modeling Research for the Crystalline Repository Project, Annual Report, FY-1986*, EG&G Idaho, Inc., for the Office of Crystalline Repository Development.

Mitchell and Gauthier, Assoc., Inc., *Advanced Continuous Simulation Language (ACSL), Reference Manual*, Box 685, Concord, MA 01742, 1986.

Paillet, F. L. and W. S. Keys, "Applications of Borehole Geophysics in Characterizing the Hydrology of Fractured Rocks," *Proceedings, National Water Well Association Subsurface Investigations Conference, San Antonio, February 1984.*

Plumb, R. A., A. Brie, and K. Hsu, "Fracture Detection and Evaluation Using New Wireline Methods," *Proceedings of the 26th U.S. Symposium on Rock Mechanics, Rapid City, SD, June 1985*, pp. 227-228.

Priest, S. D. and J. A. Hudson, "Estimation of Discontinuity Spacing and Trace Length Using Scanline Surveys," *International Journal of Rock Mechanics and Mining Science and Geomechanics, 18*, pp. 183-197, 1981.

Raven, K. G. et al., "Field Investigations of a Small Groundwater Flow System in Fractured Monzonitic Gneiss," *Proceedings International Association of Hydrogeologists Symposium on Hydrogeology of Rocks of Low Permeability, Tucson, January 1985*, pp. 72-86.

Romm, E. S., *Flow Characteristics of Fractured Rocks* (in Russian), Nedra, Moscow, 1966.

Segall, P. and D. D. Pollard, "Joint Formation in Granitic Rock of the Sierra Nevada," *Geological Society of America Bulletin*, 94, May 1983, pp. 563-575.

Rasmussen, T. C., "Three-Dimensional Computer Model of Flow and Transport in Variably-Saturated Fractured Rock," *Eos Transactions, American Geophysical Union, 67*, 44, November 4, 1986, p. 962.

4. DUAL-PERMEABILITY MODEL: LABORATORY AND FRACSL-VALIDATION STUDIES

Laurence C. Hull
Tom M. Clemo
Idaho National Engineering Laboratory

4.1 Introduction

Simulation of geothermal reservoirs for the purpose of performance assessment or location of injection wells is complicated by the fractured nature of many geothermal reservoirs. Recent advances in simulation of flow and tracer transport through fractured media may make simulation of these complex geothermal systems feasible for industry. Modeling of fractured media has been based on two primary approaches, continuum and discrete. In the continuum approach, the fracture system is divided into representative elementary volumes (REVs). The requirement for this division is that each of the REVs be sufficiently large so that effects of individual fractures cannot be distinguished in the response of the model. The scale must be large enough that the fractured rock can be treated as homogeneous.

The discrete approach represents the opposite end of the spectrum. All fractures that are considered relevant are modeled explicitly. Fractures are either described deterministically from knowledge of individual fractures in the system, or are a stochastic realization based on a statistical description of the fracture system. Discrete fracture models provide great detail on flow and transport, but require large amounts of core and time on a computer. Currently, these requirements limit discrete fracture approaches to systems with few relevant fractures or to small portions of larger fracture systems. Discrete fracture models are being used to develop properties of REVs for continuum models of fracture systems (Dershowitz, 1984; Long, 1984; Schwartz et al., 1983).

A third approach to reservoir-scale simulation of fracture systems is the dual-permeability approach (Miller, 1983). The dual-permeability approach combines the best features of continuum and discrete approaches. The most important fractures in the system are treated discretely, with the remainder of the fractures and rock matrix incorporated into representative elements. This approach reduces the computer burden, does not require homogeneity within the representative elements, and retains the flow, transport, and thermal properties of all elements in the reservoir. Development of representative element properties from fracture system characteristics is currently under way (Clemo, 1986).

In the FRACSL code, representative elements are currently modeled using an equivalent porous medium and a Gaussian dispersion model. To study the behavior of dual-permeability systems, and to validate the computer algorithms in the FRACSL code for the special case of porous-media matrix, a laboratory physical model was constructed. The model consists of two sets of discontinuous, orthogonal fractures in a porous matrix material. Dye and tracer tests have been conducted in the model and results correlated using the FRACSL code.

4.2 Model Design and Construction

In a dual permeability system, fractures occur in a permeable rock matrix. The first step in construction of the physical model was selection of an appropriate permeable matrix material. A broad range of materials was considered, including sintered glass, sintered metal, glass and plastic beads, natural rocks, porous ceramic, and porous polyethylene. To evaluate these materials, selection criteria were developed. These criteria included cost, ability to see tracer movement, size, availability, high electrical resistance (for concentration measurement), homogeneity, and hydrologic characterization. Based on these criteria, two materials were selected for further evaluation: porous ceramic and porous polyethelene.

Porous ceramic plates are available commercially on a custom order basis in sheets 30.5 x 15.25 x 1.25 cm. The thickness was obtained by building up two thinner layers. This left a high permeability zone down the center of the sheet, which would be parallel to the flow direction, making it unacceptable for physical models.

Porous polyethelene is available in sheets 1 m x 1 m x 2 cm, with an average pore size of 40 microns. The material can be machined easily, permitting a fairly complex fracture system to be designed. Sealing the surfaces of the model proved to be a bit of a problem because few materials wet polyethelene, which is necessary for good bonding. The method selected for

sealing the model was to cast the constructed fracture network into a monolith of epoxy resin.

Figure 4.1 shows the layout of the model. To emphasize the interaction between fractures and matrix, a number of dead-end fractures were included in the flow system. The fractures were generated by milling the polyethelene into various shapes and combining them like pieces in a jigsaw puzzle. Dead-end fractures were generated by cutting into the polyethelene with a sabre saw. Brass shim stock was placed between the pieces during construction so that the fractures would have a known aperture. The shim stock was removed just before final casting of the model in resin. Because epoxy resin shrinks when curing, the fractures were compressed and, therefore, fracture apertures are unknown.

Piezometers were installed in fractures and matrix blocks to measure pressure distributions. Holes were drilled through the casting resin and 1.5-mm copper tubes cemented flush with the upper surface of the model. Platinum electrodes, 3.2 mm in diameter, were embedded flush to upper and lower model surfaces to measure tracer concentration changes (specific conductance) without disturbing the flow field. Measurements of fluid conductance are made by multiplexing the electrodes with a computer controlled data aquisition system.

Flow is controlled by constant head reservoirs and syringe pumps (Figure 4.2). Constant head boundary conditions are created by using constant head reservoirs at the inlet and outlet of the model. Injection at constant flow rates is accomplished by using a syringe pump. For most tests, a steady background flow field is established through the model between constant head reservoirs. Then a tracer solution is injected through a piezometer.

4.3 Model Characterization

The physical model was characterized in two phases: the first, to characterize the hydraulic and transport properties of the porous polyethelene; the second, to characterize the hydraulic properties of the network. This second phase was necessary to evaluate fracture apertures, because this information was lost when the model was cast into resin.

4.3.1 Characterization of the Porous Polyethelene. To determine the hydraulic and transport characteristics of the porous polyethelene, a small model was constructed. A block of porous polyethelene was cut 15.24 cm wide, 10.16 cm long, and was the full 2.03 cm thickness. This block was imbedded in epoxy resin with manifolds on the two 15.24-cm sides of the block (Figure 4.3). Electrodes were imbedded in the resin 7.94 cm from the inlet side. Hydraulic conductivity of the porous polyethelene could be determined

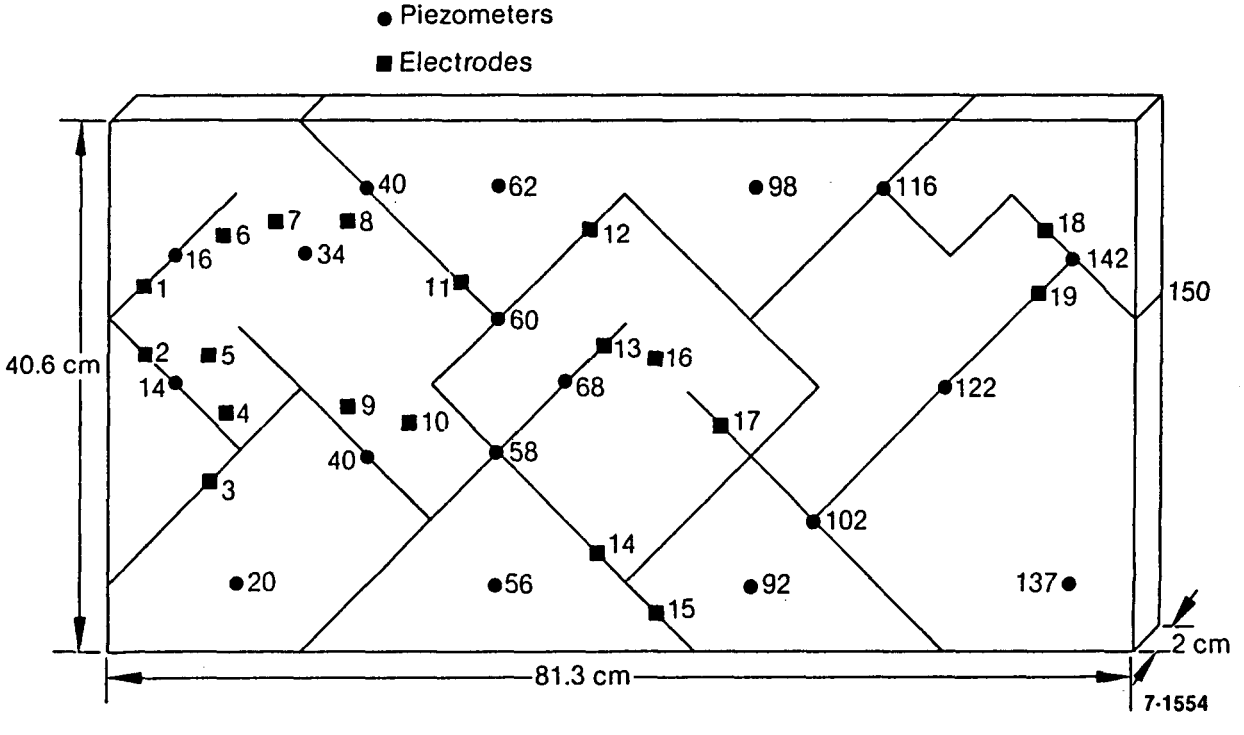

Figure 4.1. Design of dual-permeability fracture network showing locations of electrodes, piezometers, and fractures.

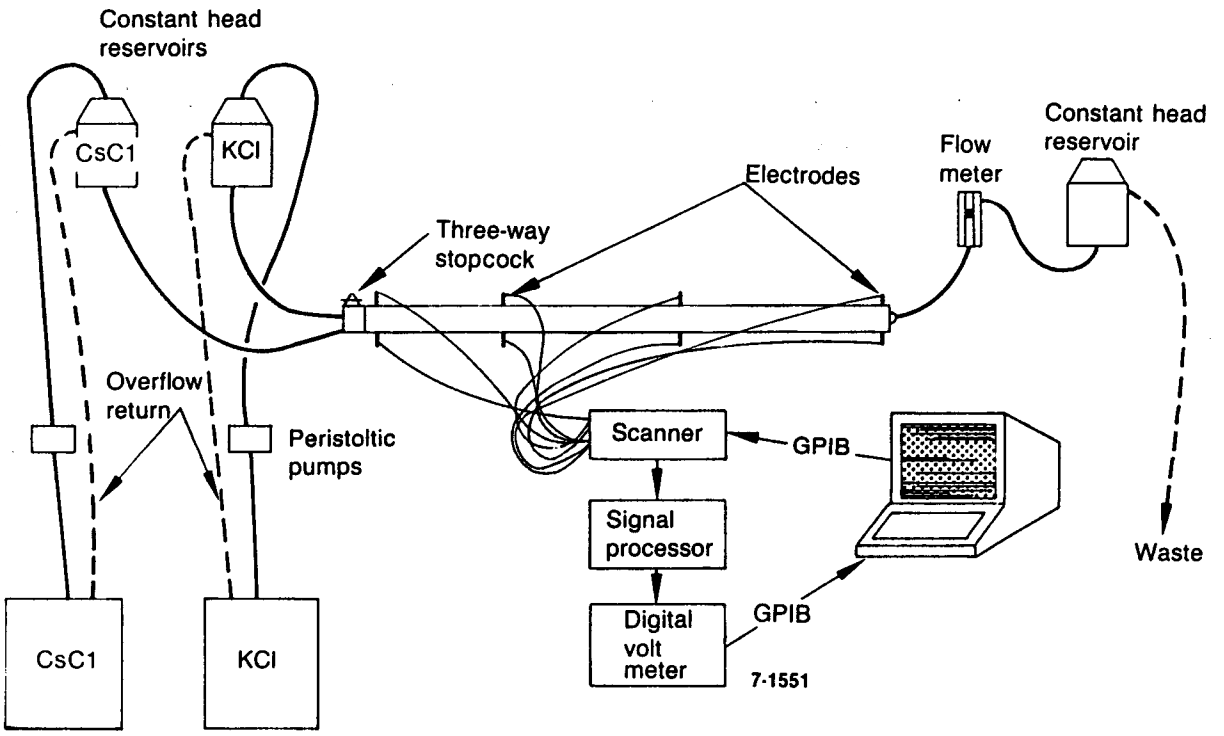

Figure 4.2. Schematic of laboratory test apparatus.

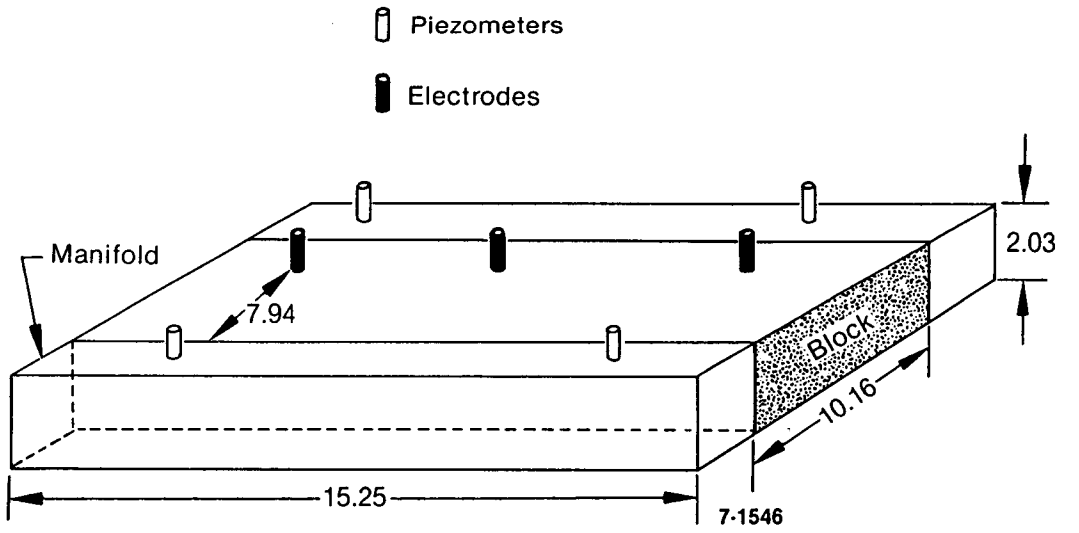

Figure 4.3. Block model used to determine hydraulic and dispersion properties of the porous polyethelene.

from pressure drop between the two manifolds and dispersivity determined by measuring tracer breakthrough at the electrodes.

Flow tests were conducted over a range of volumetric flow rates from 1.7 to 32 cm^3/min (Table 4.1). This resulted in head losses in the model ranging from 1.1 to 18.5 cm. Hydraulic conductivity of the model was determined by a least squares fit of volumetric flow rate as a function of pressure drop (Figure 4.4). The resulting equation is

$$Q = 1.62\ d\phi = 0.53\ A\ d\phi/dz. \qquad (4.1)$$

A series of tracer tests were conducted in the model to measure tracer breakthrough curves. These curves were fit using the one-dimensional advection dispersion equation (Ogata and Banks, 1961) to determine porosity and dispersivity of the porous polyethelene (Figure 4.5). The equation used to fit the data is

$$c/c_o = \frac{7}{2}\,\mathrm{erfc}\,\frac{1 - V_i/V_p}{2(PeV_i/V_p)^{1/2}} + \frac{1}{2}\exp(Pe)\,\mathrm{erfc}\,\frac{1 + V_i/V_p}{2(PeV_i/V_p)^{1/2}} \qquad (4.2)$$

Equation (4.2) has two parameters which were determined by the curve fitting routine. The first parameter is V_p, which is the pore volume of the model. This was used as a fitting parameter so the porosity of the porous polyethelene could be estimated. Direct measurements of porosity gave values on the order of 35%, but an independent estimate was desired. The second parameter is the Peclet number (Pe). The Peclet number is defined as the advection to dispersion ratio:

$$Pe = vz/D_l. \qquad (4.3)$$

The porosity of the porous polyethelene and the dispersion coefficient were calculated by using the two estimated parameters combined with physical measurements on the cross-sectional area of the model, the volumetric flow rate, and the distance to the electrodes.

Six tests were conducted over a range of volumetric flow rates from 0.046 to 17.4 cm^3/min (Table 4.2). Figure 4.6 shows the variation in dispersion coefficient with pore velocity. The dispersion coefficient is the product of the pore velocity and the dispersivity length of the matrix material. A least squares fit on the data shown in Figure 4.6 results in a dispersivity length of 0.366 cm. Effects of molecular diffusion were negligible. The average porosity of the model, based on the six tests, is 37.3%, slightly higher than measured on small blocks of material. Because the porous polyethelene does not wet, filling all the pores for measuring porosity was difficult. Therefore, the slightly higher value is used as the best number for porosity.

4.3.2 Characterization of the Dual-Permeability Network. The hydraulic characteristics of the completed fracture network had to be evaluated to determine effective fracture apertures for the dual permeability model. Fracture apertures were determined by forcing a match between the head distribution in

Table 4.1. Hydraulic characterization data for the porous polyethelene material

Date	Flow (cm^3/min)	Delta H (cm)
10/17/84	11.6	6.5
	21.3	11.4
	32.2	18.4
	22.4	12.8
	3.3	1.7
10/29/84	17.3	10.7
	14.2	9.0
	13.1	7.9
	10.1	6.4
	1.7	1.1
	22.2	13.7
11/15/84	5.2	1.3
	10.6	6.4
	11.2	6.8
	12.8	7.8
	18.2	11.0
	22.4	13.1
	1.8	1.2
11/20/84	3.9	2.4
	1.9	1.1
	8.0	4.9
	11.5	6.9
	15.7	9.1
	18.6	11.2
	23.2	13.8
12/04/84	20.0	12.8
	17.0	11.4
	14.0	9.2
	11.0	7.0
	3.2	2.0

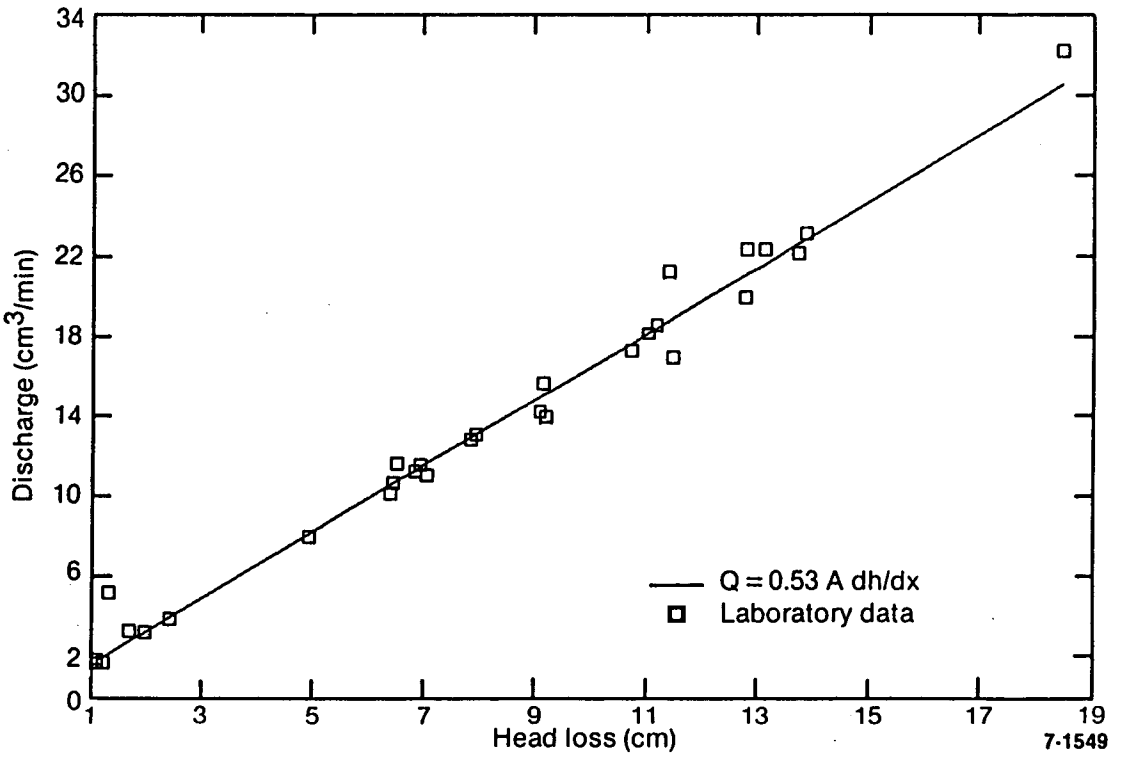

Figure 4.4. Relation of volumetric flow rate through the porous polyethelene block model to pressure drop across the model.

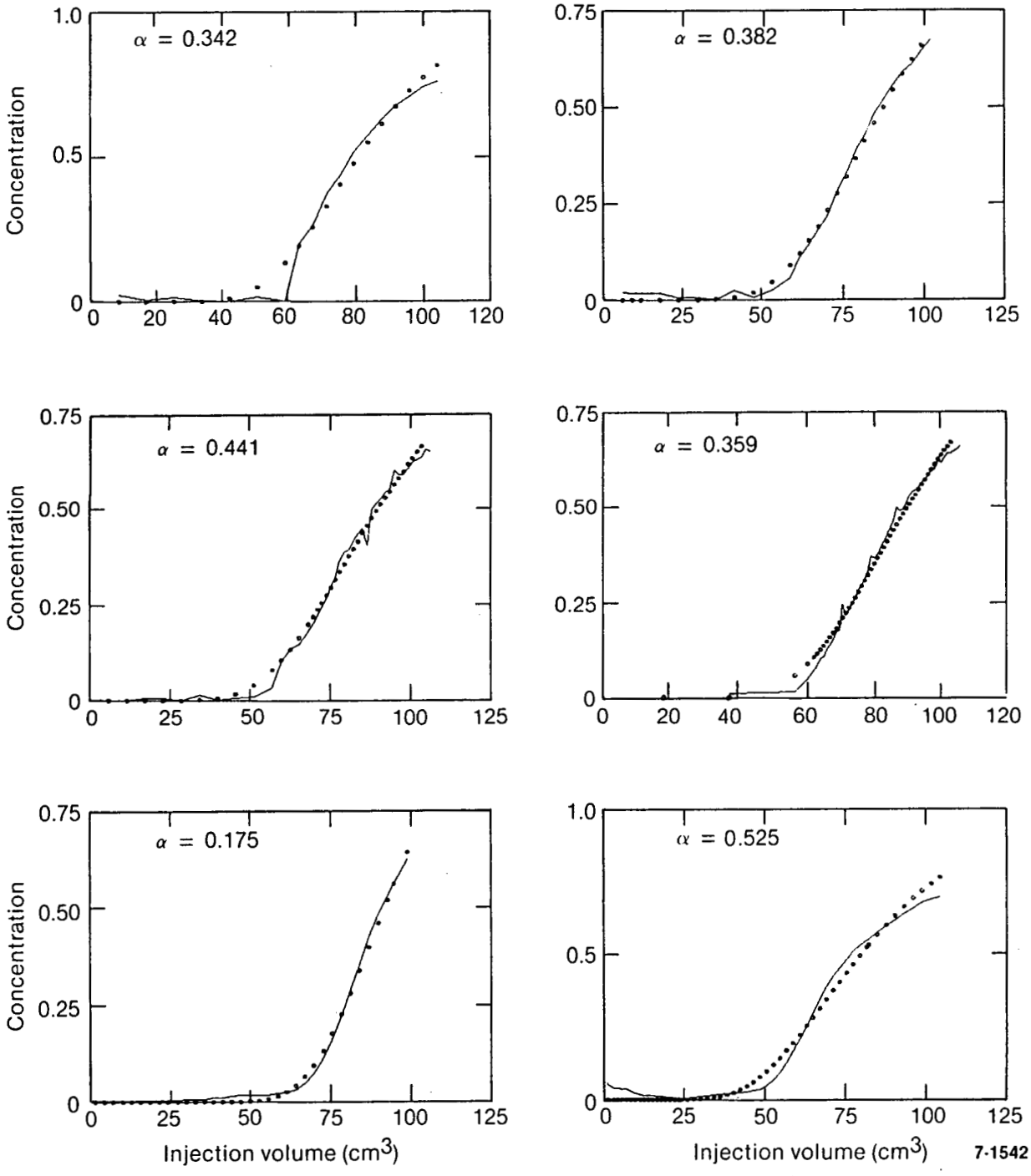

Figure 4.5. Tests conducted to determine the dispersion properties of porous polyethene. The solid lines represent the laboratory data, and the points the least squares fit of Equation (4.2) to the data.

Table 4.2. Dispersion characterization data for the porous polyethelene material

Date	Flow (cm^3/min)	Pore Velocity (cm/min)	Dispersion Coefficient (cm^2/min)	Dispersivity Coefficient (cm)
11/19/84	17.4	1.52	0.52	0.342
11/19/84	12.1	1.06	0.40	0.382
11/19/84	5.8	0.51	0.22	0.441
11/10/84	3.9	0.34	0.12	0.359
11/29/84	0.29	0.025	0.004	0.175
12/07/84	0.05	0.004	0.002	0.525

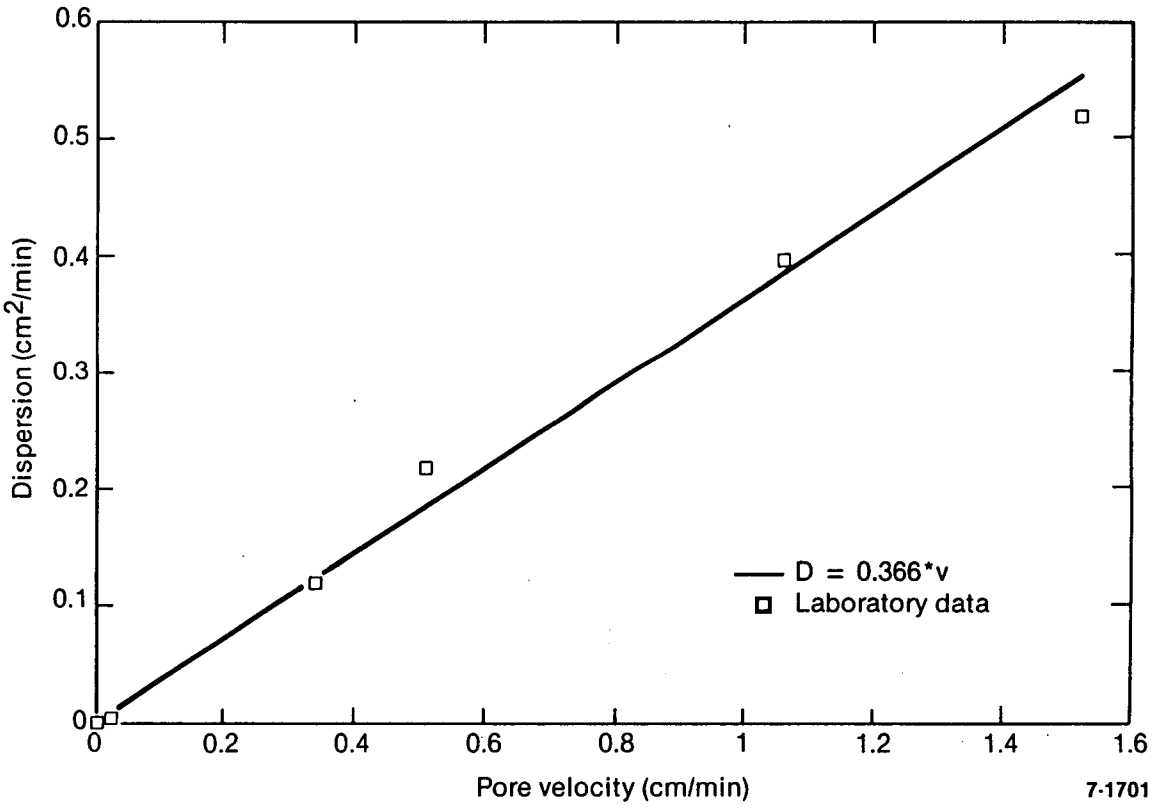

Figure 4.6. Relation between the hydrodynamic dispersion coefficient and pore velocity in the polyethelene block model. The slope of the line is the dispersivity coefficient.

FRACSL and the physical model. A series of hydraulic tests was conducted on the laboratory model and the relation between flow and pressure was measured for the piezometers in the physical model. The FRACSL code was then used to match the measured pressure distribution in the model by adjusting the apertures in the code. Figure 4.7 shows the final results of the fitting operation. Points marked with an 'M' are located in the matrix while points marked with an 'F' are located in a fracture. The final fit is very good, but the distribution of apertures is not necessarily unique. The relation between the initial, measured fracture apertures and the apertures used in the simulation are shown in Table 4.3.

4.4 Physical Model Testing

The native reservoir solution used in testing was 0.84×10^{-4} molar CsCl, with a specific conductance of 13.8 micromhos/cm^2. The tracer solution was 2.27×10^{-4} molar KCl with a specific conductance of 35.2 micromhos/cm^2. The two solutions have contrasting conductivities, but have the same density.

A number of tests were conducted; detailed results from only one test are presented here. The test consisted of injecting a mass of tracer into a matrix block (piezometer 34, Figure 4.1) while holding constant head at the inlet port and at piezometer 142, which are both in fractures. The background flow field from the inlet node to piezometer 142 was 4.55 cm^3/min. Tracer was injected at a rate of 2.63 cm^3/min for 76 minutes. During injection, outflow from the model increased to 5.07 cm^3/min. A food color dye was added to the solution to allow visual monitoring of the tracer migration along with electronic monitoring. Electrodes were scanned periodically to record conductance, and maps were drawn of the visual indications of the tracer front.

Figure 4.8 shows the maps of the tracer plume at various times during the test. The maps are qualitative, in that a diffuse boundary is drawn as a single line on the map. This is particularly true of the trailing edge of the plume, where significant dispersion was occurring. The drawings were taken from the top surface of the physical model. Viewing the bottom of the model revealed that the leading front on the bottom was similar, but not identical, to the plume location on the top. This is an indication of some density effects in the tracer movement introduced by using the dye to permit visual observation of the tracer.

The plume initially moved out in a fairly typical radial pattern, which was only slightly affected by

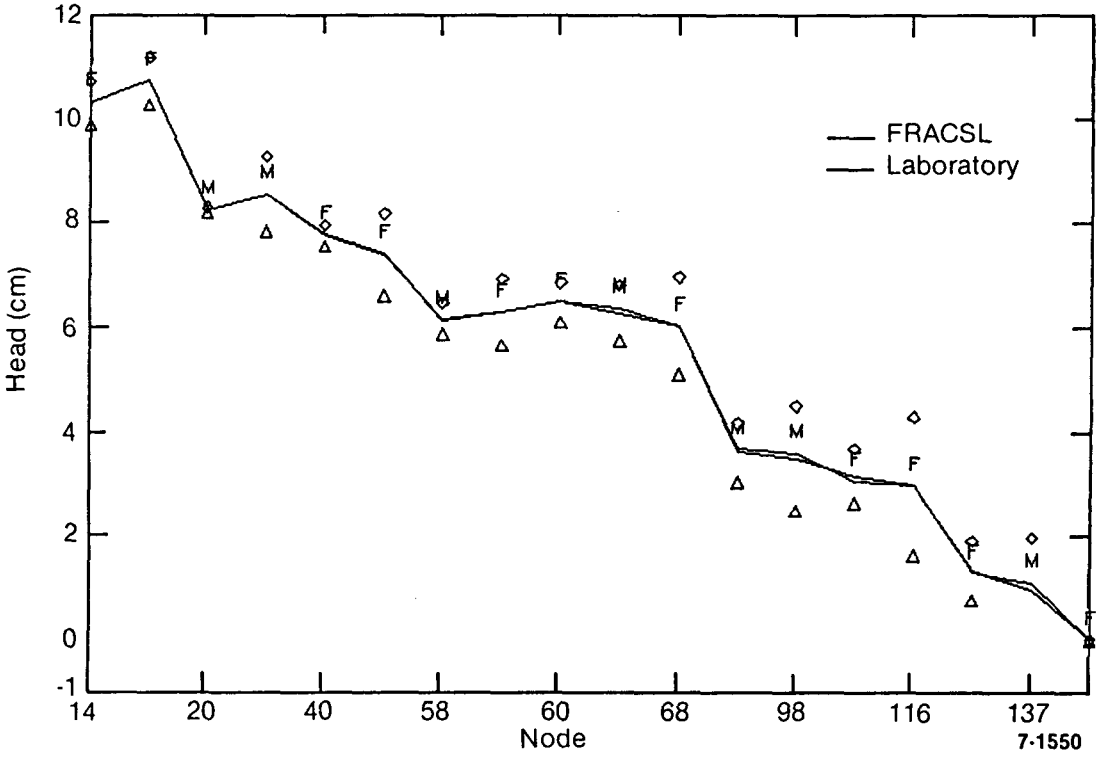

Figure 4.7. Correlation of predicted piezometric heads in the FRACSL model to measured pressures.

Table 4.3. Measured and estimated fracture apertures for the dual-permeability model[a]

	Aperture (microns)			Aperture (microns)	
Fracture	Measurement	Estimate	Fracture	Measurement	Estimate
1	1140	1140	24	640	130
2	1140	1140	25	1020	100
3	1270	350	26	890	220
4	1140	100	27	1080	220
5	890	150	28	1270	1270
6	890	150	29	510	230
7	640	70	30	1020	1000
8	760	500	31	1020	260
9	890	800	32	890	260
10	890	180	33	1520	1140
11	890	140	34	1520	1140
12	890	140	35	380	300
13	890	230	36	890	250
14	640	500	37	760	220
15	510	510	38	640	300
16	510	350	39	380	90
17	510	350	40	380	70
18	510	350	41	380	70
19	510	470	42	760	50
20	510	120	43	760	90
21	760	450	44	760	150
22	760	450	45	760	300
23	640	130	46	640	130

a. Because of shrinkage of the casting resin, there is not necessarily a relation between the two numbers. Measured apertures are ± 64 microns.

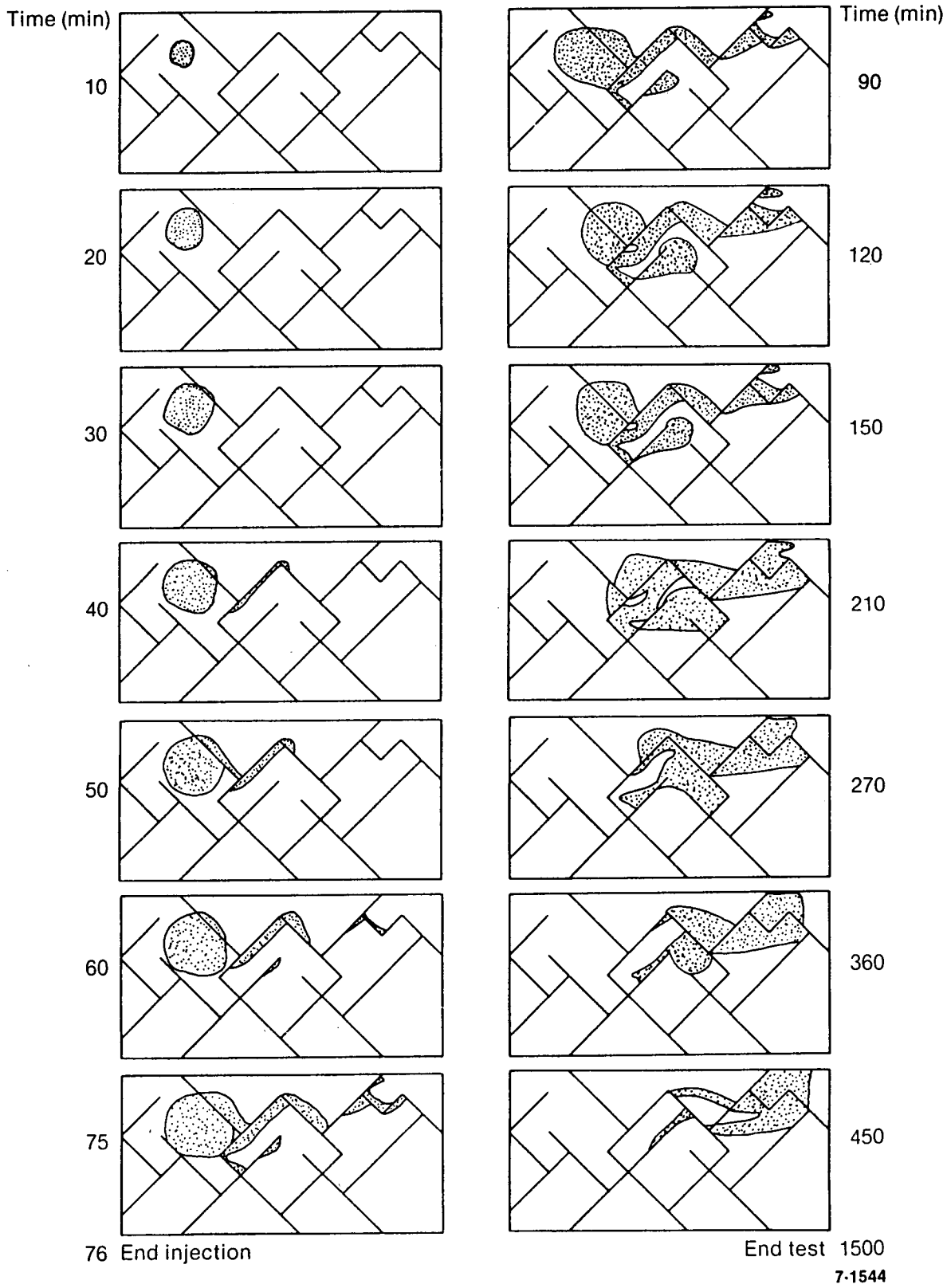

Figure 4.8. Maps of tracer distribution in the physical model.

interception of the diagonal fracture at 30 minutes. Significant amounts of tracer were transferred to matrix material adjacent to the fractures and flowed roughly parallel to those fractures.

A plume continued to grow around the injection node for the 76-min injection period. After injection ended, the plume moved from left to right toward the withdrawal node. The plume retained a great deal of its initial shape to about 150 min. At that point, the plume was greatly distorted by fractures and became much more elongated. The plume's retention of its original shape while crossing a fracture indicates the low permeability of the fractures in that portion of the physical model.

Once the tracer plume crossed the centerline of the model (210 min), the shape of the plume broke up, and complex interactions between the fractures and matrix developed. Significant amounts of tracer-bearing fluid transfer from fractures to down-gradient matrix. Details of plume shape reveal the effects of individual fractures. At 210 and 270 min, a tongue of native fluid can be seen moving through the central block. This tongue appears to originate from fracture 16 (see Figure 4.9), where native fluid moves more rapidly down the fracture while tracer remains in the matrix material on either side of the fracture.

4.5 FRACSL Validation

The tracer test conducted on the physical model was simulated using the FRACSL code. The simulation was performed to validate the flow and transport algorithms in FRACSL. A number of significant improvements in the algorithms were made during this validation effort. The code provides tracer location maps, which can be compared to visual observations; the code also provides time-concentration plots, which can be compared to electrodes imbedded in the model. The concentration of tracer leaving the model is recorded and can be compared to electrode response at the outlet. In general, the code performs very well. The tracer position plots closely to the maps made during the tracer tests. The electrode responses also agreed with the test data but not as closely as the visual plots.

4.5.1 FRACSL Model Definition. Figure 4.1 provides a schematic of the model geometry. Each intersection of the horizontal and vertical lines represents a node. The heavy lines represent the fractures and are numbered as shown, with the longer fractures being comprised of several shorter segments. The numbered circles show the locations of electrodes. To simulate the tracer tests, node 34 and node 142 were defined to have fixed flow rates. The cross flow was introduced by fixing a constant head at the boundary node, node 6. Each of these nodes is labeled appropriately in Figure 4.9. The edges of the model were treated as no-flow boundaries.

The material properties are those determined for the polyethylene, as presented previously. A general

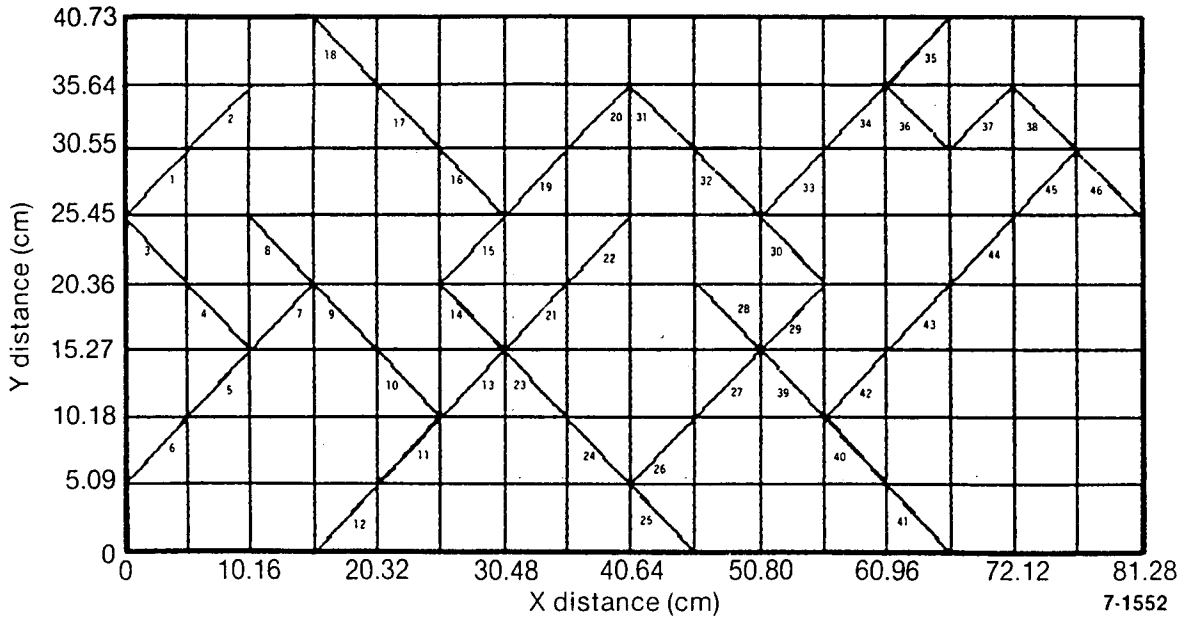

Figure 4.9. Layout of the dual-permeability fracture network used in FRACSL showing the finite difference grid and the fracture numbering system.

parameter sensitivity study will be performed during FY-1987. All matrix properties were assumed to be uniform throughout the physical model. The fracture positions exactly match those of the physical model, while the fracture apertures are based on fitting pressure measurements rather than the original measurements of the model.

4.5.2 Comparison of Particle Locations to Tracer Plots. Figure 4.10 presents the tracer particle location plots resulting from the FRACSL simulation using measured polyethylene properties. These plots can be compared to Figure 4.8, which contains hand-drawn boundaries of the tracer as observed in the physical model.

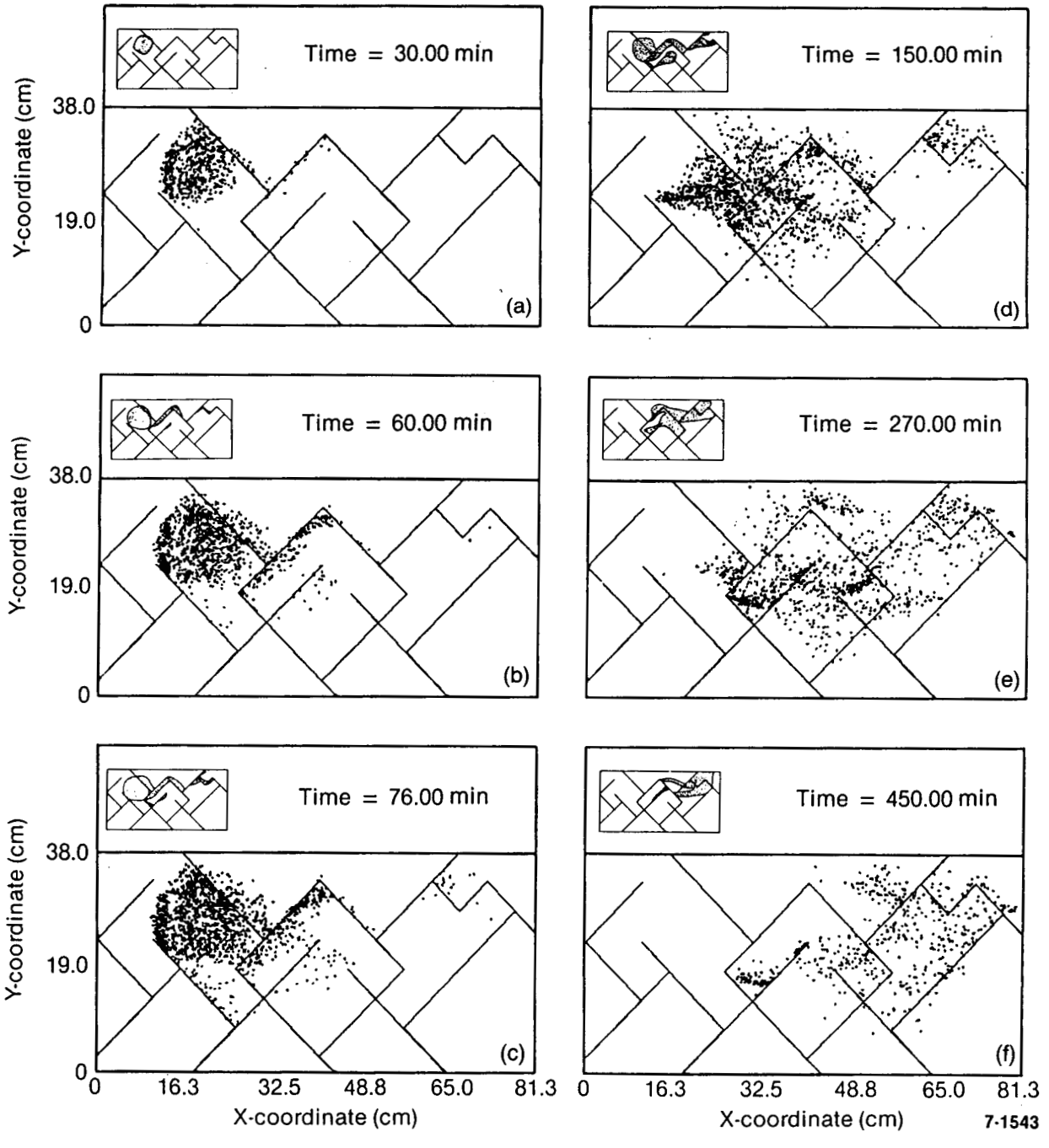

Figure 4.10. Maps of tracer location simulated using the FRACSL code.

Figure 4.10a presents the particle positions 30 min into injection. The plot is identical to the drawing of the tracer. Figure 4.10b is for 60 min into injection. It shows a well-developed front below fractures 19 and 20, and a few particles have crossed fracture 31. Particles transferring from fracture 22 to the adjacent matrix block travel farther than the tracer map in Figure 4.8 indicates. This region, however, showed the most marked difference between top and bottom surfaces of the physical model. Therefore, the map based on the test data may underestimate the extent of tracer movement in the central block. Figure 4.10c (76 min) can be interpreted similarly to Figure 4.10b. Particles appear in the matrix near fractures 9 and 10, which were not observed in the physical model. The particles are so sparse that the tracer here may have been overlooked. Another area of difference is a lack of particles leaving fractures 33 and 34 in the simulation.

The presence of clean water sweeping the tracer out of the injection region is evident in Figure 4.10d (150 min). Because of the diffuse nature of the tracer front, this was not picked up in the drawings of the tracer plume (Figure 4.8). The region to the right of fractures 16, 17, and 18 shows an open strip adjacent to and down gradient of the fractures. Fracture 8 intercepts flow moving through the central portion of the model and provides a screen for fluid sweeping out the injection region. This is evident by the hangup of particles in this region. This phenomenon could have been overlooked in mapping the plume in the physical model. During a subsequent test, when tracer was injected into node 34, the hangup of tracer in the region of fracture 8 was observed.

The particle plot for 270 min (Figure 4.10e) indicates that the particles have not moved as far as the tracer appeared to. This is especially evident in the region to the right of fracture 14. It is possible that the simulated flow in fracture 14 is larger than in the physical model. This could shield the region downgradient from the fracture in the same manner as occurs for fracture 8. The plot also indicates particles in the region between fracture 29 and fracture 43, which was not evident in the test. This could indicate an improper flow split between fractures 19 and 22.

The final plot in Figure 4.10 shows the simulated particle distribution of tracer at 450 min. There is very good agreement between the simulated and mapped tracer distributions. Both show the tongue of native fluid cutting through the matrix in the central block and to the right of fractures 31 and 32. The one area where the two plots differ is between fractures 29 and 43. The code simulates too much tracer in this region, possibly by permitting too much flow to move out of fracture 29.

4.5.3 Comparison of Electrode Responses. The simulated electrodes all exhibit a rough agreement with the test data. Generally, the shape and timing of the simulation agrees well with measured results. The magnitude of the response, however, is widely different from the test results in some cases. All the time versus concentration plots in Figure 4.11 are for normalized tracer data. Test data are normalized by subtracting the conductance of the CsCl tracer from the measurements and dividing the result by the difference in conductance between the CsCl and KCl tracers. Simulation results were normalized by introducing a tracer with unit concentration at the injection port.

Figure 4.11a presents both the simulated response and the measured response of electrode 7. Electrode 7 is located in the center of matrix element 25 (Figure 4.9), just upstream of the injection port. The FRACSL simulated tracer breakthrough starts earlier but reaches a similar normalized concentration as the measured response. A similar effect is seen for electrode 8 (Figure 4.11b), with the simulation preceding the tracer response.

In Figure 4.11c the simulated and measured response of electrode 11 are very similar. Because electrode 11, which is located at the midpoint of fracture 16, is influenced by far fewer particles than electrodes 7 and 8, the calculated response is much noisier. In Figure 12c the simulated response is heavily averaged and still shows large fluctuations. The simulated response rises earlier but drops at about the same rate as the measured response.

Figure 4.11d, the response of electrode 12, appears to show very poor agreement between the simulated and measured responses. Electrodes 13, 16, and 17 (Figures 4.11e, f, and g) also do not show a close agreement between simulation and measurement. These plots reveal that, for the simulation, too much of the tracer travels through the central block of the model. The general timing of the response at the electrodes agrees closely, but the magnitude is very different. The distribution of flow around the central block is different in the simulation than in the laboratory model. Much more flow travels through the block in the simulation. This results in the lower concentration at electrode 12 for times greater than 200 min and the consistently overestimated concentrations for electrodes 13, 16, and 17. Another effect of the flow-split mismatch is the presence of tracer in the region between fractures 29 and 43 (see Figure 4.10d).

Electrode 18 (Figure 4.11h) shows an excellent match between simulated and test data. Figure 4.11i indicates a reasonable match between simulation and measurement for electrode 19. Figure 4.11j plots the response of electrode 20, which was situated in the outlet stream of the model. The measured data reveal

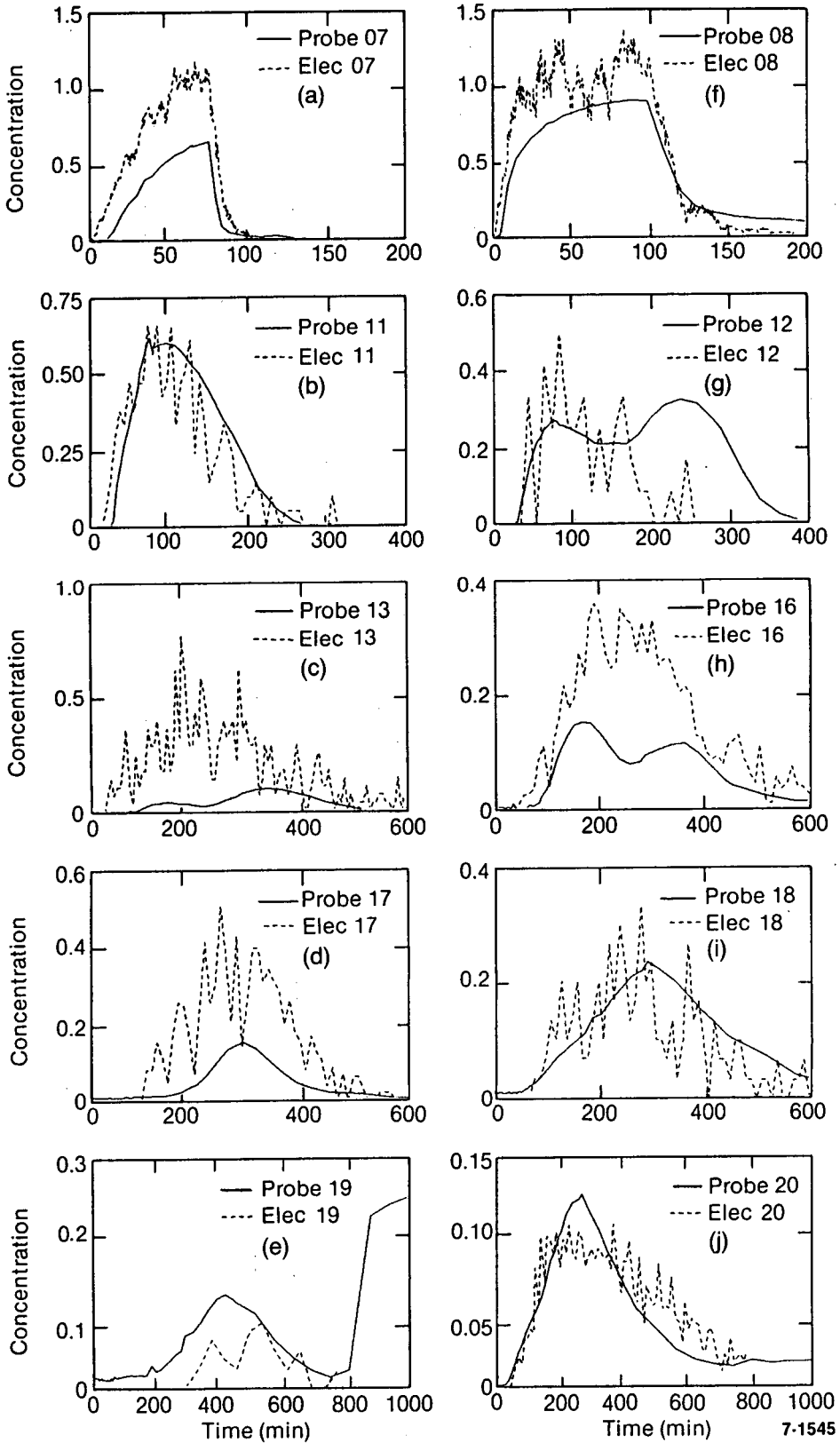

Figure 4.11. Comparison of tracer breakthrough curves measured in the laboratory with curves predicted using the FRACSL code.

a sharper peak than the simulation shows. The spread in the simulation may be the result of more flow through the central matrix block than around the block in fractures.

4.5.4 Discussion. In terms of both spatial distribution and temporal variation, the FRACSL simulation does a reasonable job of matching the laboratory data. Because of uncertainties in fracture apertures, there are places where the FRACSL simulation is not correctly simulating the flow field in the physical model. Two places where this is most evident are in the central block of the model on both sides of fractures 21 and 22 and also between fractures 29 and 43. This is an example of a situation where, although the pressure response is matched very well, there is not an equally good match to the actual fluid movement in the model.

4.6 Code Improvements

Simulation of the dual permeability model has been the first attempt to compare FRACSL to laboratory data in which both fractures and the matrix play an important role. The comparison revealed areas in the code that required improvements. These areas have been addressed in the course of providing simulations of the laboratory experiments. The improvements to the code can be divided into four areas. These areas are the mass balance routine used to calculate the pressure response, the calculation of the transverse (cross) flow in fractures, a new routine to model transport at the fracture-matrix interface, and a change to the movement of particles within the matrix. The net effect of these improvements is to increase the efficiency and accuracy of the code.

4.6.1 Mass Balance Routine. The routine for calculating the pressure derivative (mass balance) at nodes was based on a linear pressure distribution. This assumption had previously been dropped for the particle movement calculations and replaced with a more accurate second-order pressure profile assumption. The calculation of the nodal pressure response has been upgraded to be consistent with the particle movement routine.

The new mass balance calculation uses the particle movement coding to calculate the nodal mass balance by calculating the velocity of pseudo particles at eight locations on the nodal volume boundary. These locations are depicted by the arrows labeled QS in Figure 4.12. The locations are the midpoints of the outer boundaries of each of the four quadrants making up a nodal volume. These velocities provide a more accurate estimate of the net flow across the nodal volume boundaries than the previous routine. The new

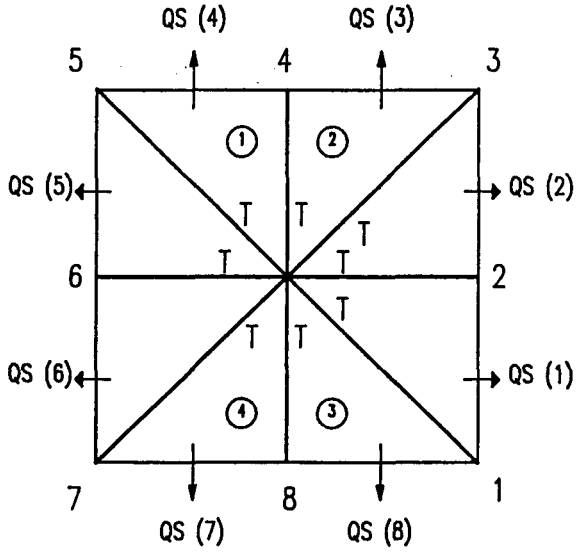

Figure 4.12. Schematic of a nodal volume as used in the FRACSL code showing the locations where fluid transfer between nodes is calculated for computing the mass balance.

routine is more time consuming than the first order routine but results in a slight decrease in the code's memory requirements. The net effect is a tradeoff of increased computing time for improved accuracy.

4.6.2 Transverse Fracture Flow. Detailed study of the flow fields calculated for the simulation of the dual permeability model revealed that a tighter correlation was needed between the calculation of flow leaving the sides of fractures and the flow leaving the nodal boundaries. The flow leaving through fracture walls had been determined from the velocity of a pseudo-particle placed just outside the edge of the fracture, halfway between the node and the edge of the nodal volume. This velocity was assumed to be constant for the portion of the fracture in the nodal volume. The sum of the flows through fracture walls should equal the sum of the fluid accumulating in the node and the flow out of the node. For the dual permeability model, the deviation between the two flow calculations was deemed unacceptable.

The transverse fracture flow now makes use of the results of the mass balance calculation, which forces agreement between the two. Figure 4.12 depicts a nodal volume in which all possible locations of fractures have been highlighted with heavy lines; these fractures have been numbered 1 through 8. Note that the flow across a boundary is calculated between each possible fracture location. The net flow leaving the node between two fractures is apportioned equally

between the fractures. The transverse fracture flows are subsequently adjusted for flow leaving one fracture and entering the second without crossing the nodal boundary by calculating the velocity of a pseudo particle midway between the fractures. A final adjustment of the flows is made by equally apportioning the net accumulation of fluid within the node to the fractures. This procedure guarantees the fluid leaving the fractures balances with flux leaving the node and the accumulation of fluid within the node.

The transverse flows calculated are constant for each fracture within a given node. Modification of the routine to provide linearly varying velocities would make the fracture transport calculations conceptually closer to the matrix movement routine. The modification could be a future upgrade to the FRACSL code.

4.6.3 Fracture-Matrix Interface. The random walk approach is the most fundamental method of stochastically simulating the diffusion mechanism. Random walk is an implementation of the theory of Brownian motion. Diffusion is simulated by moving discrete tracer particles in a random direction, with equal probability in each direction, a distance which is normally distributed. The variance of the distance moved is proportional to the length of time of the move. The net movement over a fixed period of time is independent of the time step. The probability distribution for a single move is depicted in Figure 4.13.

Figure 4.14 shows the movement of a particle from point A to B. Although this is a single movement in the simulation, the particle does not travel from A to B in a direct path. In fact, the velocity of the particle is everywhere discontinuous. Figure 4.15 presents the same movement from A to B in time steps which are 1.0% of the original. This property of Brownian motion becomes important if a particle is moving from one environment to another where the diffusion is affected. The fracture wall is an example of an environment change. In Figure 4.15 the particle cannot move from A to B in the manner shown if line C-C′ represents the wall of a fracture and the shaded area represents the matrix material. The random walk technique can thus introduce error into the diffusion

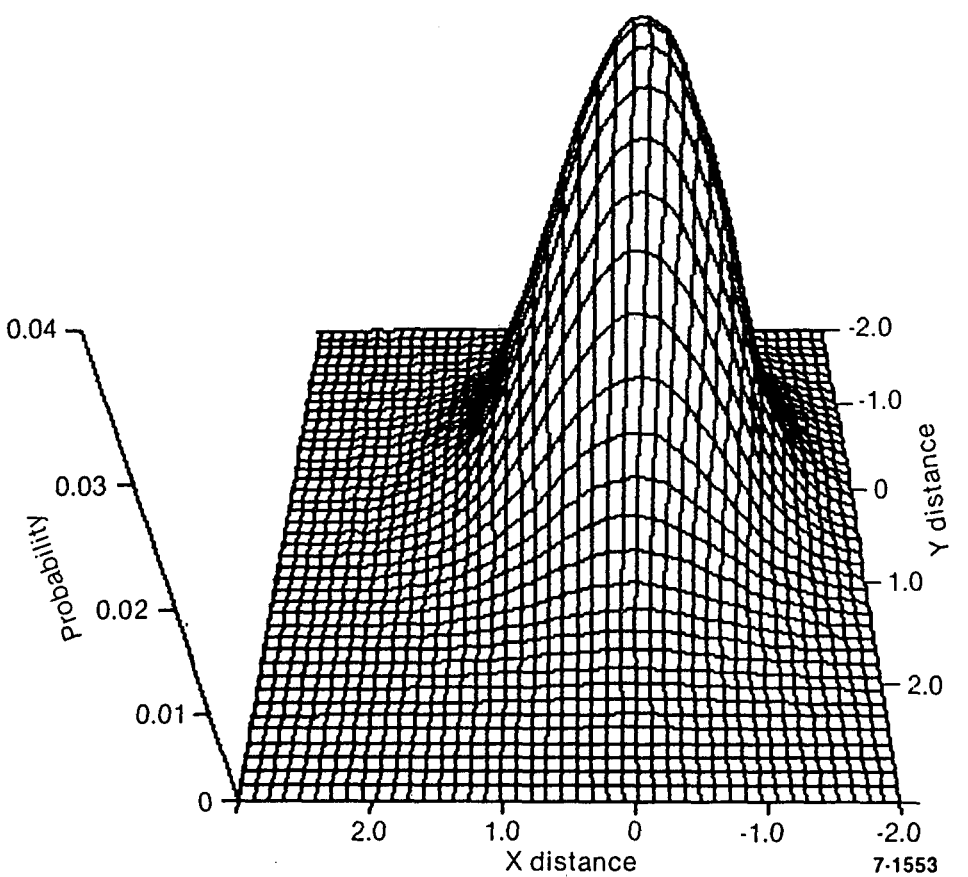

Figure 4.13. Two-dimensional probability density function used to predict solute transport using the Random-Walk approach.

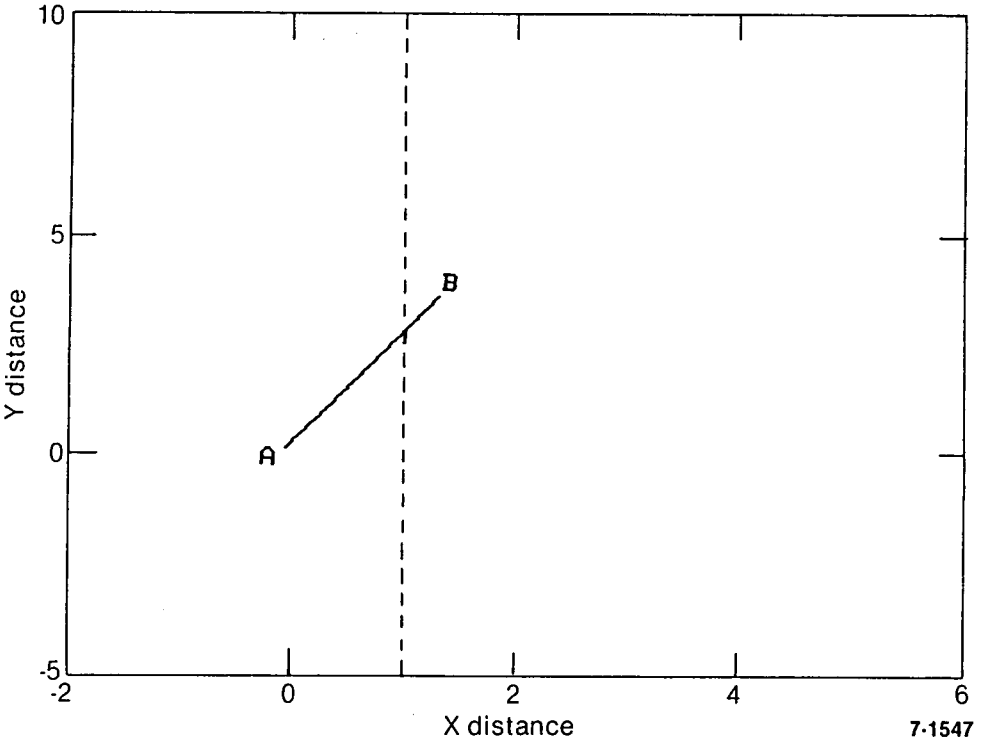

Figure 4.14. Movement of a particle by diffusion for a time step Δt.

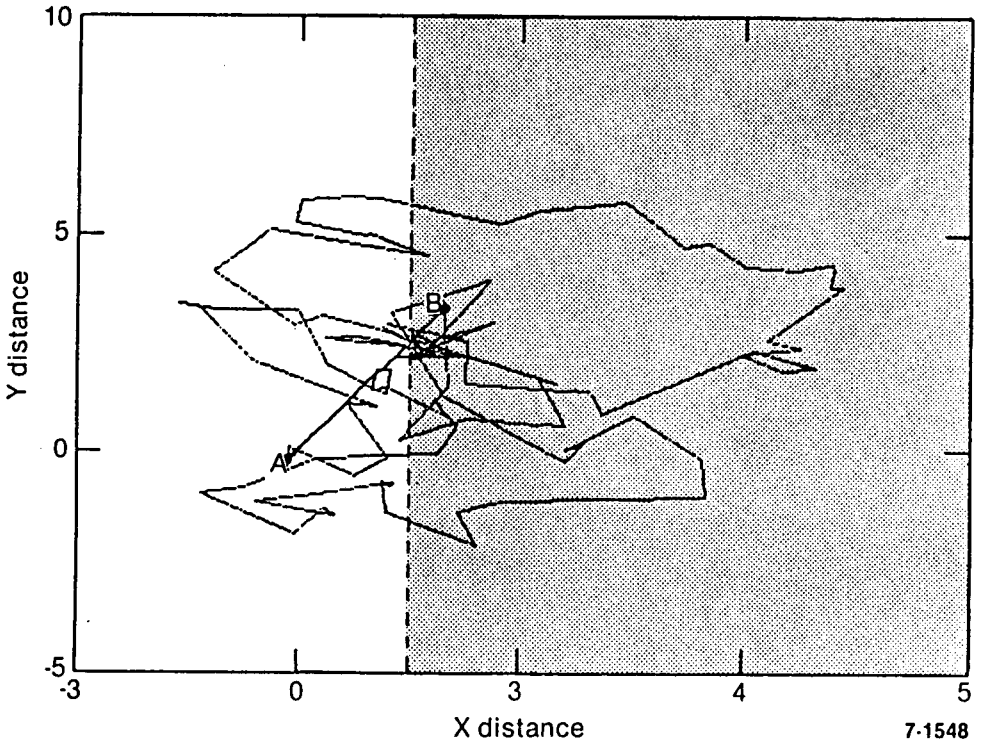

Figure 4.15. Movement of a particle by diffusion for 100 time steps of length Δt/100.

simulation. This error can be controlled, but not eliminated, by reducing the time step. Unfortunately, the cost of simulating movement is inversely proportional to the time step used. A mechanism to directly simulate interaction with the fracture wall both eliminates the error source and greatly reduces the cost.

Changes were made to the FRACSL code to accommodate solute diffusion into the matrix material from fractures and vice versa. The fracture transport algorithm was modified to include a special case if diffusive movement is large compared to the aperture of the fracture. This criteria is determined from the Peclet number for a fracture which is defined by

$$Pe = 210\ D_m L/vb^2. \qquad \text{(Hull, 1985) (4.4)}$$

The special routine is used if the fracture Peclet number is greater than 200.

This routine overrides the normal time step limit based on diffusion. Instead, the net effect of diffusion is treated stochastically. Particles move longitudinally down the length of the fracture at the average fluid velocity in the fracture. During movement down the fracture, a particle will strike the walls numerous times due to diffusion. Occasionally, the particle will find an opening in the the wall and enter the matrix material. In the vast majority of these cases the particle eventually diffuses back into the fracture. The routine calculates the probability of the particle reaching a specified distance into the matrix. A Monte Carlo routine is used to determine if a particle reaches this distance away from the fracture and the length of time used to get there. Having reached this distance, the particle is considered to have transferred to the matrix.

Calculating an overall probability is more efficient than the previous scheme of monitoring each time the particle strikes the wall. The efficiency of the code can be controlled by optimizing the selection of the distance needed to diffuse into the matrix before a transfer is made. This distance has been chosen so that, on the average, a particle will diffuse out to this distance a few times over the period of time it takes to reach the end of the fracture.

In the matrix, a particle near a fracture is also treated specially because of the previously described effects of an environment change introduced into the particle movement near the fracture. This problem has been solved analytically, resulting in a Macro Monte Carlo implementation of the particle movement. A single calculation is performed both in terms of transfer to the matrix or the final position of the particle if it remains in the matrix. Macro Monte Carlo refers to the one-step calculation of transition or position rather than following the random walk behavior of a particle.

The modifications were motivated by erroneous behavior of the original modeling. It was found that the transport into and out of the matrix was affected by the time step used in FRACSL. The modifications have not only corrected the original problem but have resulted in a significant reduction in the cost of moving particles in a diffusion-dominated situation.

These modifications are consistent with a shift in the philosophy about the level at which the random nature of particle movement should be addressed. Our investigations are leading us into ever-increasing complexity. In order to limit the FRACSL code to reasonable size and cost, the solute transport algorithms must be as sophisticated and efficient as possible. Modeling transport on a higher level than the pure random walk approach requires an up-front cost in analytical development.

4.6.4 Matrix Movement Modification. A new subroutine has been created which makes the movement of particles in the matrix more efficient. A major problem with the movement routine occurred when a particle crossed a matrix element boundary. After crossing a boundary, the particle was positioned a trivial distance away from the boundary. The likelihood of a particle diffusing back across the boundary was great, even with a strong advective flux. This problem caused particles to spend an inordinate amount of time crossing and recrossing boundaries due to diffusion. The excess time did not affect the accuracy of the results but substantially increased the cost per particle of moving in the matrix.

The new subroutine allows particles to overshoot the matrix element boundaries if such an overshoot would not degrade the accuracy of the calculations. This places the particles away from the element boundaries and free from artificial diffusion dominance.

Figure 4.16 is a schematic of the region which controls particle movement in unfractured matrix. The dots represent the nine nodes that influence the movement of a particle. The particle exists in one of the four quadrants bounded by the dashed lines. These four quadrants make up a nodal volume. Each quadrant is located in a separate matrix element. Each time a particle crosses the boundaries (dashed lines) a new velocity and velocity derivative are calculated. If the particle moves from one of these quadrants to another, it enters a new matrix element. If the two elements are the same material, then the velocity calculations are identical, and no error is introduced by overshooting the element boundary. If the boundary between the elements does not contain a fracture, then the particle may continue movement in the new quadrant without recomputing the velocities.

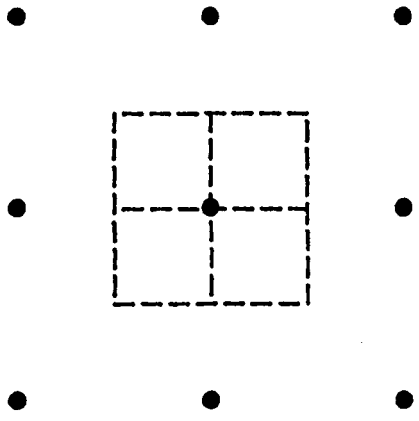

Figure 4.16. Nodes used to calculate the pressure gradient and velocity vectors for particle motion.

The routine also allows a slight overshoot when a particle crosses an outer boundary of the dashed region. This introduces an error in the movement routine because the spatial derivative of the particle changes at the boundary. Keeping the overshoot small limits the error to an acceptable amount. The overshoot can be justified by considering the source of the changes in velocity. Once the particle crosses the quadrant boundary, new nodes contribute to the velocity calculations. These nodes and the nodes lost to the calculations are all far away from the particle and, hence, contribute little to the velocities. The gain in efficiency outweighs the loss in accuracy.

4.7 Conclusions

Innovative approaches to simulation of flow and transport in complex fracture systems will have to be developed before computer techniques can be used in performance assessment of geothermal reservoirs. The dual-permeability approach is one such innovative technique that can be used to simulate complex fracture systems with reasonable allocation of computer costs and core storage. The technique has been validated by using a small-scale laboratory model of a dual-permeability fracture system.

FRACSL simulations of the laboratory model showed good agreement with data collected from the model in terms of the pressure distribution and overall rate of tracer movement. In a few places, differences in predicted tracer movement from measured movement are caused by uncertainties in the fracture apertures in the model. Destructive evaluation of the model to measure fracture apertures will be performed when no further use of the model is envisioned. The magnitude of tracer response in the model and in the FRACSL simulations differed by a large amount in a number of cases. Some of this difference can be attributed to FRACSL not measuring the concentration of tracer in matrix material surrounding electrodes located in fractures.

A number of improvements have been made to the code to increase its net efficiency and accuracy. The most significant improvement is the implementation of a Macro Monte Carlo algorithm for simulation of transport in fractures and transfer from fractures to matrix. This algorithm steps up a level from simulating the basic transport processes to predicting the outcome of a number of processes occurring over a fixed time interval, and it represents a significant advance in the FRACSL code.

4.8 Bibliography

Clemo, T. M., "Representative Element Modeling of Fracture Systems Based on Stochastic Analysis," *Eleventh Workshop on Geothermal Reservoir Engineering, Stanford University, January 1986.*

Dershowitz, W. S., *Rock Joint Systems*, unpublished Ph.D. Thesis, Massachussetts Institute of Technology, Cambridge, MA, 1984.

Hull, L. C., *Physical Model Studies of Dispersion in Fracture Systems*, EG&G-ELS-6845, Idaho Naional Engineering Laboratory, Idaho Falls, ID, April 1985.

Long, J. C. S., *Verification and Characterization of Continuum Behavior of Fractured Rock at the AECL Underground Research Laboratory*, BMI/OCRD-17, LBL-14975, Lawrence Berkeley Laboratory, Berkeley, CA, 1984.

Miller, J. D., "A Fundamental Approach to Flow and Transport in Fracture Systems," *Proceedings: Ninth Workshop on Geothermal Reservoir Engineering, Stanford University, 1983*, p. 379.

Ogata, A. and R. B. Banks, "A Solution of the Differential Equation of Longitudinal Dispersion in Porous Media," *Professional Paper 4ll-A*, U.S. Geological Survey, Reston, VA, 1961, pp. A1-A7.

Schwartz, F. W., L. Smith, A. S. Crowe, "Stochastic Analysis of Macroscopic Dispersion in Fractured Media," *Water Resources Research, 19*, 5, 1983, pp. 1253-1265.

5. TRACER DEVELOPMENT: EXPERIMENTAL STUDIES

Michael C. Adams
Joseph N. Moore
University of Utah Research Institute
Salt Lake City, Utah

5.1 Introduction

In most geothermal fields, the spent brines must be injected back into the reservoir. The purposes of injection are to maintain reservoir pressure and to avoid subsidence and environmental pollution. However, injection can lower the temperature of the producing fluids in a field by mixing with the hotter formation fluids. In order to mitigate this problem, the subsurface paths of the injected fluids must be known. Tracers can be used to label and track fluid movement and monitor changes in the chemistry of the injected fluid (Wright et al., 1984). Despite their potential importance to the geothermal operator, very few tracers are presently available and of those that are available, little is known about their stabilities or behavior at the elevated temperatures that typify resources capable of electric power generation. During the past 2 years, the University of Utah Research Institute has been involved in the development and testing of chemical tracers for geothermal use. The results of this research are presented below.

5.2 Tracer Development

The ideal tracer should be detectable in small quantities, nonreactive with reservoir rocks and fluids, inexpensive, environmentally safe, and absent from natural geothermal fluids and ground waters. The tracers currently in use in high-temperature environments fall into three major categories: (a) radioactive isotopes, (b) salts of iodide and bromide, and (c) organic dyes. Each of these classes of tracers has significant limitations.

Radioisotope tracers should be limited to those not used as natural process tracers, such as ^{3}H and ^{36}Cl. In addition, the half-life of the tracer must be of a suitable duration so that errors from decay corrections are kept small. An additional drawback to the use of radioactive tracers is their toxicity. For example, the tracer used during injection tests at the Wairakei and Broadlands geothermal fields, ^{131}I, is one of the more toxic radionuclides (McCabe et al., 1983).

The salts, although relatively stable and inexpensive, are limited by the high background of halides in many geothermal systems, requiring large quantities of salt for adequate tracer detection. In addition, because most of the salts are compounds of Na, K, Li, and Mg, they interfere with cation geothermometry of the fluids (Adams, 1985).

The most significant restriction in the use of organic dyes is their lack of diversity. Only one species, fluorescein, has been used with complete success in injection tests (Adams, 1985; Adams et al., 1986; Tester et al., 1986). However, laboratory tests conducted by UURI during 1986 indicate that fluorescein degrades rapidly at temperatures above 250 to 300°C, as discussed in Section 5.5.8. Rhodamine WT has been used with limited success at Klamath Falls, Oregon (Gudmundsson et al., 1983) and Svartsengi, Iceland (Gudmundsson et al., 1984).

The lack of diversity among the commonly used tracers restricts the number of wells that can be individually monitored in a producing field at one time. Thus, in geothermal fields where several injection wells are in use, it is not possible to independently trace the movement of fluids injected into each well.

Hydrocarbons and their derivatives are a new class of tracers now being tested that may meet all of the requirements, including diversity. Four substitutional groups of hydrocarbons are currently being studied. These are the ring fluorinated, trifluoromethylated, sulfonated, and methyl- or carboxylated groups. The substrates for the substitutions are benzene, benzoic acid, and phenylacetic acid.

The salts of substituted benzoic acids were originally selected for use in ground water studies (Bentley, 1982) because these salts possess many of the required characteristics of the ideal tracer (Davis et al., 1980; 1985). These compounds are negative ions at the pHs of natural ground waters and are therefore nonsorbing. They are low in toxicity, especially in the range of concentrations needed for monitoring studies (ppb to ppt), and they are available as a large suite of similar species. The addition of fluorine to the benzene ring lends greater resistance to microbial degradation, with resistance increasing directly with the degree of fluorine addition. As a result, several fluorinated benzoic acids—particularly pentafluorobenzoic acid, p-fluorobenzoic acid, and m-(trifluoromethyl)benzoic acid—have been used extensively in ground water studies.

One of the objectives of our tracer program is to extend the use of tracers to vapor-dominated systems. Therefore, we have included potentially stable tracers with a variety of volatilities in our experiments. If the distribution coefficients between the steam and liquid are known, then the subsurface processes can be elucidated. To this end, we have also been testing the sulfonic, acetic, and methylated derivatives.

5.3 Experimental Procedures

The experimental runs were designed to produce a rapid evaluation of the thermal stabilities of many hydrocarbon derivatives. In the initial set of experiments, five ground water tracers were tested at 125 to 150°C to determine if any were thermally stable at even moderate temperatures. These tracers were tested in the presence of an atmospheric as well as a nitrogen gas phase. Based on the success of these experiments discussed below, 34 other compounds were added to the next set of experiments, which were run at 250°C. The 250°C experiments were also run with an atmospheric or nitrogen gas phase. Subsequent experiments were run at 200°C in the presence of only a nitrogen gas phase because of the rapid decay of the compounds in oxygen at 250°C.

The experiments at 125°, 150°, and 250°C were each run for 1 week. Longer-term runs have only been performed at 200°C. Five of the compounds initially selected were deleted from these experiments because it was felt that degradation products from their rapid decay were interfering with identification of the tracers during analysis. These compounds were the pentafluorobenzoic, pentafluorobenzenesulfonic, p-(trifluoromethyl)phenylacetic, 3,5-(trifluoromethyl) phenylacetic, and 2,6-difluorobenzoic acids.

Five experimental reaction vessels were put into operation during 1985. These vessels are housed at the University of Utah's Department of Metallurgy. One vessel is capable of sustaining temperatures up to 350°C. The use of multiple reaction vessels makes it possible to perform experiments of relatively long duration on several different tracers or under different conditions simultaneously.

At the beginning of each experiment, 30-mL aliquots of the solutions containing the tracers are encapsulated in sealed quartz tubes (Figure 5.1). The ampules are sealed in an oxymethane flame. Approximately 2 mL of the ampule are occupied by a gas phase during each experimental run. The gas phases used for these experiments are either pure nitrogen or ambient atmosphere (about 20 vol% oxygen). The solutions in the experimental runs with nitrogen as the gas phase are purged with nitrogen gas in the ampule for up to 2 hours. During sealing, the neck of the ampule is aspirated to prevent oxygen contamination from the oxymethane flame. Oxygen concentrations were measured for several solutions, and these averaged 6.9 ppm O_2 in the atmosphere-equilibrated solutions, and from 0.27 to 0.05 ppm in the nitrogen-equilibrated solutions, depending on the purge time.

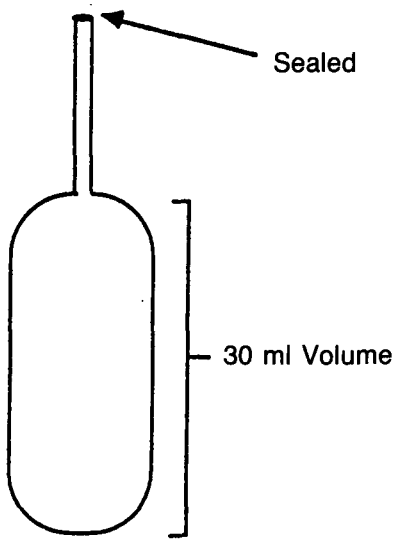

Figure 5.1. Annealed quartz vial used to contain the tracers in a closed system during hydrothermal experiments.

Several preliminary experiments were run during 1986 on tracer stability in the presence of altered rock. The tracer used was fluorescein because of the ease and speed of analysis. The rocks used were drill chips from well MC-1 of the Meager Creek British Columbia geothermal system. These rocks are moderately altered quartz diorites. Quantitative chemical and mineralogical composition of the rocks were not obtained after each run because the purpose of the experiments was only to develop our experimental method. A significant problem encountered in the studies was removing adsorbed oxygen from the rocks prior to emersion in the tracer solution. This was finally accomplished by twice boiling the rock in distilled water under nitrogen until dry and then adding the tracer solution. The tracer solution was also purged with nitrogen before and after it was added to the experimental vial.

5.4 Analytic Methods

Analysis of hydrocarbon concentrations down to 20 ppb can be achieved by direct injection of up to 0.2 mL of sample into a high-pressure liquid chromatograph (HPLC). On-column enrichment techniques

can be used to lower detection limits if needed (Stetzenbach et al., 1982). For HPLC analysis of the benzoic acids, the eluant buffer was prepared by adding sufficient phosphoric acid to reduce the pH to 1.9 with acetonitrile added in the 17 to 45% range. For analysis of benzenesulfonic acids, an ion-pairing reagent was added (tetrabutyl ammonium phosphate) and the pH adjusted to 6.0. A polymer-based column was used because it is more resistant to degradation than silica-based resins. Detection was by ultraviolet absorption at 200 to 205 nm. Fluorescein was analyzed using a colorimeter and a fluorometer for high and low concentrations, respectively.

Multiple determinations were performed on each sample to establish analytic errors. Standard deviations were calculated and ranged from 0.0 to 3.2%, averaging 0.94%. Recovery precision for these initial studies has tentatively been established at ±15%. Later studies will emphasize analytic methods and will reduce this to more acceptable limits.

5.5 Experimental Results

The results of the thermal stability tests are summarized in Table 5.1. A total of 25 compounds were stable after 4 weeks in distilled water in the presence of nitrogen at 200°C. At 250°C, 14 of the compounds were stable after 1 week in distilled water and nitrogen.

The tracers tested can be divided into six groups. These are mono- and difluorobenzoic acids, perfluorinated aromatic acids, trifluoromethyl-substituted acids, fluorophenylacetic acids, benzenesulfonic acids, and methyl- and carboxyl-substituted benzoic acids. The molecular structure and chemical name of these compounds are shown in Figure 5.2. Each compound is referenced to one of the stability plots by the letter shown at the upper left of each structure. Percent recovery is defined as the final concentration, divided by initial concentration multiplied by 100. The thermal stability of each group is discussed below.

5.5.1 Mono- and Difluorobenzoic Acids. Fluorinated aliphatic compounds are known to be stable with respect to biodegradation and temperature (Sheppard and Sharts, 1969); however, they are insoluble in liquid water and, therefore, are unsuitable as tracers in liquid-dominated geothermal reservoirs. Our tracer program was initially designed to test fluorinated aromatic hydrocarbons, which have a higher solubility in liquid water, are nonbiodegradable, but were untested with respect to temperature. As our research progressed, we discovered that many of the fluorobenzoic acid compounds were not stable above 200°C. Because a wide variety of tracers is needed, we added sulfonated, methylated, and carboxylated benzoic acids as potential tracers.

The stabilities of the mono- and difluorobenzoic acids with respect to time at 200 and 250°C are shown in Figure 5.3 and listed in Table 5.1. Seven combinations of substitutional positions on the benzene ring were tested. Of these seven, four had not decayed after 4 weeks at 200°C and two had not decayed after 1 week at 250°C. The relative amounts of decay of the compounds indicate that the dominant mechanism of decay is substitution of the negative ion, probably a hydroxyl, for fluoride. These data fit a mechanism commonly referred to as bimolecular atomatic substitution (see, for example, Kobrina, 1974). If this mechanism is operative, then bromide- and chloride-substituted benzoic acids will react more slowly and be more stable with respect to temperature than fluoride substitutions. Since bromo- and chloro-substituted benzoic acids are reported to be no more toxic than fluoro-substitutions future tests will include the chloro and bromo compounds as potential high-temperature tracers.

5.5.2 Perfluorinated Aromatic Acids. The results for the perfluorinated atomatic acids (Figure 5.4) indicate that they are not suitable as geothermal tracers, although they are the most widely used of the non-dye organic ground water tracers. A bimolecular aromatic substitution decay mechanism for the fluorobenzoic acids, discussed above, implies that the effects of fluoro-substitution are additive, i.e., the more fluorides on the ring the more rapid the decay. The effect of this substitution is demonstrated in Figure 5.4 by the low recoveries of the pentafluoro derivatives of benzoic, phenylacetic, and benzenesulfonic acids. Pentafluorobenzoic acid rapidly decayed at temperatures as low as 125°C.

5.5.3 Trifluoromethyl Benzoic Acids. The trifluoromethylated benzoic acids are good ground water tracers. However, as shown in Figure 5.5, most are not acceptable as tracers at temperatures of 250°C and above. While three trifluoromethylated compounds remained stable for 4 weeks at 200°C, only one survived 1 week at 250°C with more than an 85% recovery.

The data for the trifluoromethyl substituted compounds (Figure 5.5) do not show a sequence of decay that indicates bimolecular aromatic substitution. These compounds have an increase in stability with a decrease in distance between the trifluoromethyl moiety and the carboxyl group. This indicates that steric hinderance, or crowding, is the main factor preventing a rapid rate of reaction (Filler, 1970).

Table 5.1. Summary of results

Compounds Stable at 200°C (672 hours)	Compounds Stable at 250°C (168 hours)
Mono- and Difluorinated Benzoic Acids	
p-fluorobenzoic acid	m-fluorobenzoic acid
m-fluorobenzoic acid	p-fluorobenzoic acid
p-fluorobenzoic acid	
3,4-difluorobenzoic acid	
Benzenesulfonic Acids	
benzenesulfonic acid	benezenesulfonic acid
p-toluenesulfonic acid	p-toluenesulfonic acid
4-ethylsulfonic acid	4-ethylsulfonic acid
2,5-dimethylsulfonic acid	2,5-dimethylsulfonic acid
Hydrocarbons	
benzoic acid	benzoic acid
2,3-dimethylbenzoic acid	2,3-dimethylbenzoic acid
2,4-dimethylbenzoic acid	2,5-dimethylbenzoic acid
2,5-dimethylbenzoic acid	3,4-dimethylbenzoic acid
2,6-dimethylbenzoic acid	3,5-dimethylbenzoic acid
3,4-dimethylbenzoic acid	3-fluoro-5-methylbenzoic acid
3,5-dimethylbenzoic acid	isophtalic acid
3-fluoro-5-methylbenzoic acid	terephtalic acid
phtalic acid	
isophtalic acid	
terephtalic acid	
Fluorophenylacetic Acids	
o-fluorophenylacetic acid	None are stable at 250°C
p-fluorophenylacetic acid	
m-fluorophenylacetic acid	
Trifluoromethyl Benzoic Acids	
3,5-bis(trifluoromethyl)-benzoic acid	None are stable at 250°C
m-(trifluoromethyl)-benzoic acid	
Perfluorinated Benzoic, Phenylacetic, and Sulfonic Acids	
None are stable at 200°C	None are stable at 250°C

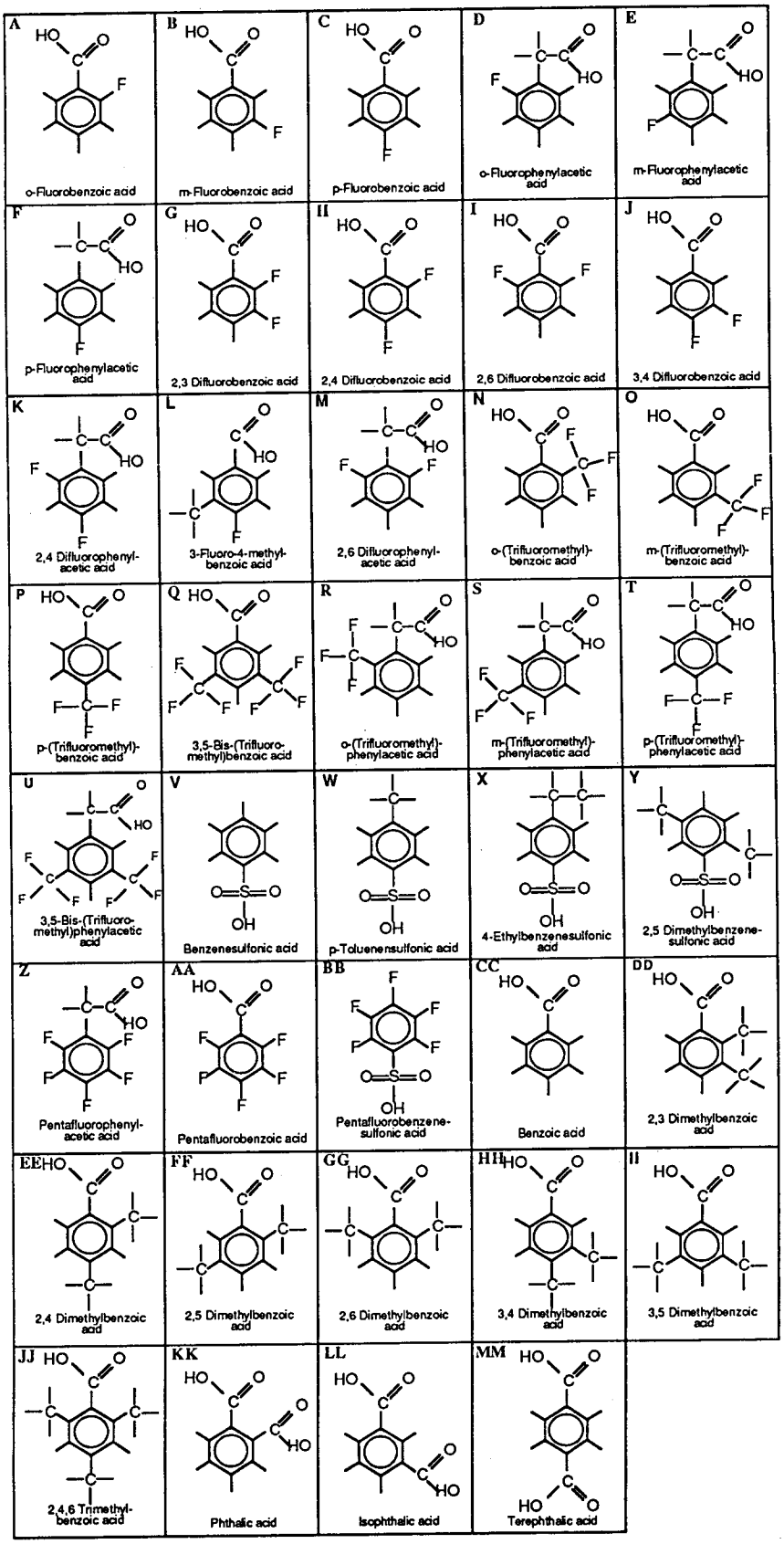

Figure 5.2. Chemical names and structures of hydrocarbon derivatives being tested.

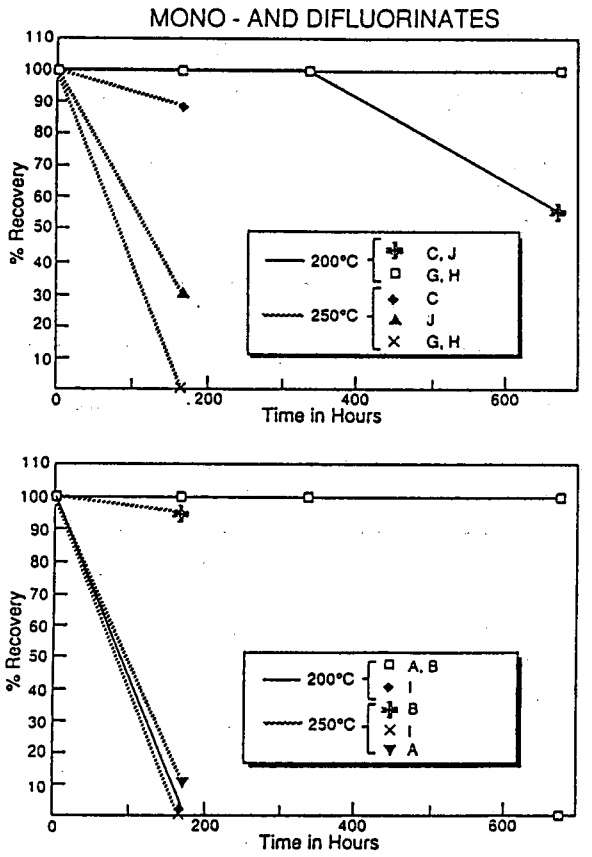

Figure 5.3. Recovery vs. time plot for mono- and difluorinated benzoic acids.

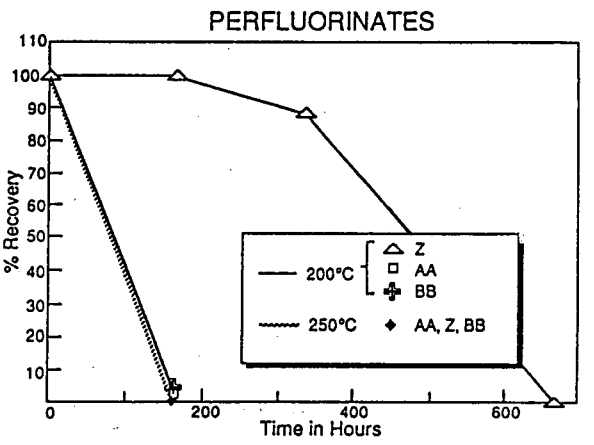

Figure 5.4. Recovery vs. time plot for pentafluorinated benzoic, phenylacetic, and benzenesulfonic acids.

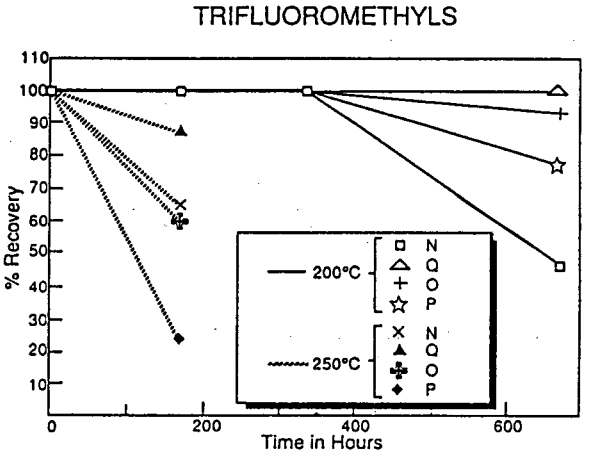

Figure 5.5. Recovery vs. time plot for trifuloromethylated benzoic acids.

5.5.4 Fluorophenylacetic Acids. Monofluoro, difluoro, and trifluoromethyl derivatives of phenylacetic acid were tested at 200 and 250°C (Figure 5.6). At 200°C the o-, m-, and p-fluorophenylacetic acids were stable for 4 weeks. At 250°C, all of the phenylacetic acids decayed below 10% of their initial recovery. The sequence of decay at 200°C indicates nucleophilic substitution.

5.5.5 Benzenesulfonic Acids. At 200 and 250°C the benzenesulfonic acids show little or no decay (Figure 5.7). Benzenesulfonic acids are heavier and more acidic than benzoic acids. These properties increase their liquid solubility and decrease their steam solubility to a greater degree than the other tracers we have tested. Thus, sulfonates are the best tracers for following the movement of liquid in a two-phase system. Where temperatures are below 100°C the benzenesulfonic acids are potentially subject to biodegradation, so that special handling procedures may be necessary, such as the addition of formaldehyde to the collected sample.

5.5.6 Methyl- and Carboxyl-Benzoic Acids. Methyl- and carboxyl-substituted benzoic acids were tested because of their nontoxic nature and expected stability. At 200°C only one out of eleven compounds decayed below 85% (Figure 5.8). At 250°C, seven out of eleven survived. The results indicate that the m- and p-positions of the methyl and carboxyl substitutions are the most stable, while the o-position is the least stable.

5.5.7 Oxygen Sensitivity. All of the compounds tested showed high rates of reaction in the presence of molecular oxygen. Figure 5.9 shows the concentrations of five representative compounds after being heated in the presence of atmospheric oxygen for

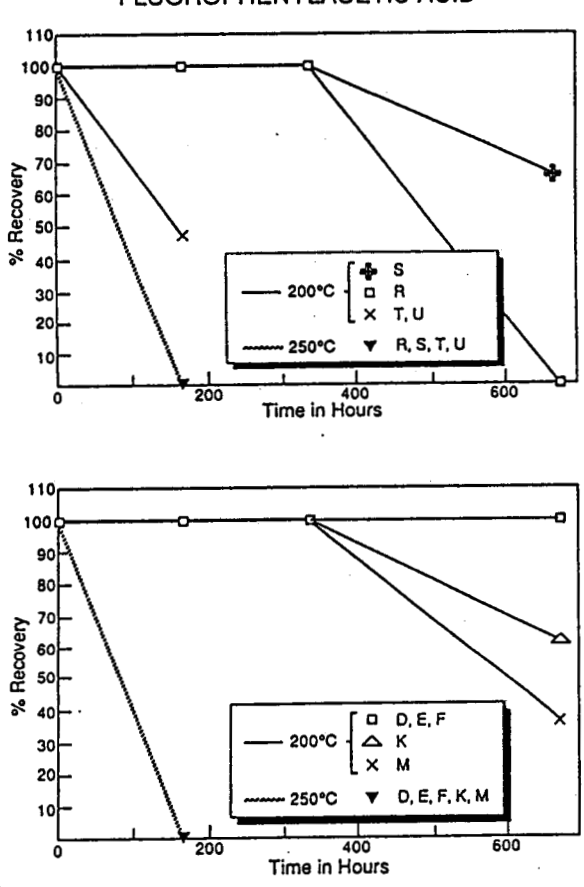

Figure 5.6. Recovery vs. time plot for derivatives of fluorophenyl-acetic acids.

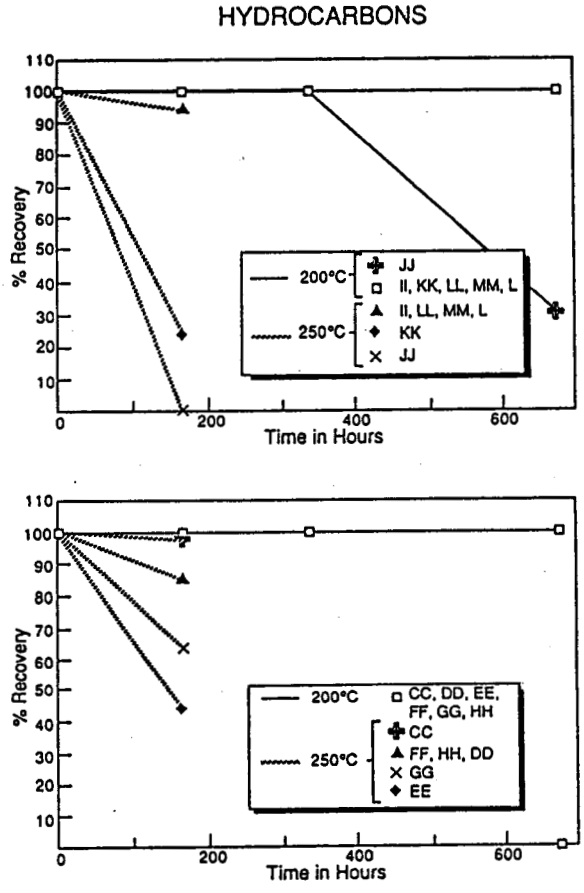

Figure 5.8. Recovery vs. time plot for methylated and carboxylated benzoic acids.

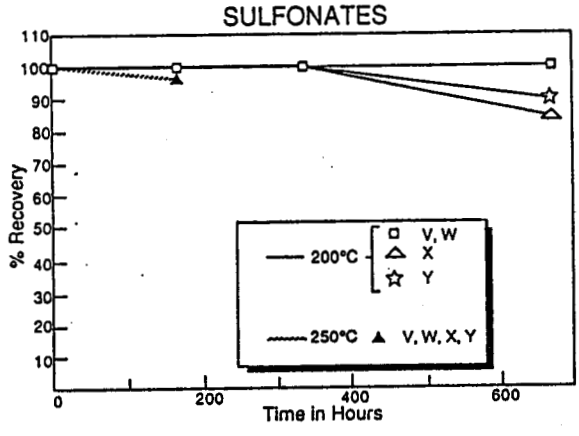

Figure 5.7. Recovery vs. time plot for derivatives of benzenesulfonic acids.

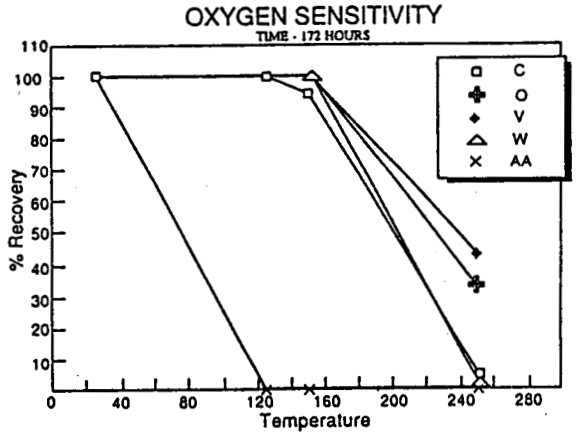

Figure 5.9. Recovery vs. temperature for five hydrocarbon derivatives in the presence of atmospheric oxygen.

approximately 1 week. It is obvious from this figure that the concentration of oxygen in the injected fluid will have to be considered in any field tracer test over 150°C. The tracers were not tested at 200°C in the presence of oxygen, but this test is planned for fiscal year 1987.

5.5.8 Rock-Tracer Interaction. Preliminary tests were carried out with altered quartz diorite and the tracer dye fluorescein at 250°C for 112 hours. Rock/water weight ratios of 0.0, 0.07, 0.20, and 0.67 were used. The mineral assemblage consisted of quartz, illite, chlorite, and epidote. This assemblage is typical of a felsic intrusive rock subjected to hydrothermal alteration at 200 to 250°C. The recovery ratios for fluorescein in these tests were 0.89, 0.89, 0.86, and 0.88, respectively. These results are identical within analytic error and indicate that the decay rate of fluorescein was not affected by the altered quartz diorite used in the experiments.

Fluorescein was also tested at 300°C. At this temperature fluorescein decays rapidly with a half-life of approximately 1 day. Analysis of the data indicates that the reaction is first order with respect to altered fluorescein. The decay rate was not affected by the presence of altered quartz diorite.

5.6 Conclusions

The thermal stabilities of 39 hydrocarbon derivatives and the tracer dye fluorescein have been tested at temperatures ranging from 125 to 250°C. The compounds were tested in distilled water for 1 to 4 weeks at molecular oxygen concentrations consistent with geothermal reservoir and surface conditions. At 200°C, 25 of the 39 compounds survived at over 85% of their initial concentrations; at 250°C, 14 survived. The most stable groups at the higher temperatures were benzenesulfonic, methylbenzoic, and carboxylbenzoic acids. Mono- and difluorinates were considerably less stable whereas perfluorinates and fluorophenylacetic acids decayed completely. Thus, a number of diverse hydrocarbon compounds are potentially suitable as geothermal tracers.

The tracer dye fluorescein was tested at 250 and 300°C in the presence of rock, with rock/water weight ratios ranging from 0.07 to 0.67. The results indicate that fluorescein is inert with respect to rock at 250 and 300°C, and decays rapidly at 300°C.

Our future studies will include: (a) testing the hydrocarbon derivatives at 250 and 300°C for 2 and 4 weeks; (b) heating the tracers in the presence of rock, CO_2, H_2S, and saline brines; (c) testing chloro- and bromo-benzoic acids for temperatures >250°C; and (d) searching for and testing tracers that are stable and usable in vapor-dominated systems.

5.7 Bibliography

Adams, M. C., "Tracer Stability and Chemical Changes in an Injected Geothermal Fluid During Injection-Backflow Testing at the East Mesa Geothermal Field," *10th Workshop on Geothermal Reservoir Engineering*, Stanford Univ., 1985 pp. 247-252.

Adams, M. C. et al., "Tracer Developments: Results of Experimental Studies," *11th Workshop on Geothermal Reservoir Engineering*, Stanford Univ., in press. 1986

Bentley, H. W., "Selection and Design of Tracers for Evaluation of Aquifer Parameters," *ACS Symposium on the Hydrology of Mining and Industrial Wastes*, El Paso, Abstracts With Program. 1982

Davis, S. N. et al., "An Introduction to Groundwater Tracers," *EPA Manual* (in review). 1980

Davis, S. N. et al., "Groundwater Tracers—A Short Review," *Groundwater, 18*, pp. 14-23. 1985

Filler, R., "Trifluoromethyl Armmatic Compounds," *Advances in Fluorine Chemistry, 6*, 1970 pp. 1-41.

Gudmundsson, J. S. et al., "Doublet Tracer Testing in Klamath Falls, Oregon," *9th Workshop on Geothermal Reservoir Engineering, Stanford Univ.*, 1983 pp.331-337.

Gudmundsson, J. S. et al., "Injection and Tracer Testing in Svartsengi Field, Iceland," *Proc. 6th N.Z. Geothermal Workshop*, 1984 pp. 175-180.

Kobrina, L. S., "Nucleophilic Substitution," *Fluorine Chemistry Reviews, 7*, 1974 pp. 3-94.

McCabe, W. J., B. J. Barry and M. R. Manning, "Radioactive Tracers in Geothermal Underground Water Flow Studies," *Geothermics, 12*, 1983 pp. 83-110.

Sheppard, W. A., and C. M. Sharts, *Organic Fluorine Chemistry*, New York: W. A. Benjamin, Inc., 1969 p. 357.

Stetzenbach, K. J., S. L. Jensen, G. M. Thompson, "Trace Enrichment of Fluorinated Organic Acids Used as Groundwater Tracers by Liquid Chromatography," *Environmental Science and Technology, 16*, 1982 pp. 250-254.

Tester, J. W., B. A. Robinson, and J. H. Ferguson, "Inert and Reacting Tracers for Reservoir Sizing in Fractured, Hot Dry Rock Systems," *11th Workshop on Geothermal Reservoir Engineering*, Stanford Univ., in press. 1986

Wright, P. M. et al., "Uses of Geochemistry with Injection-Backflow Testing in Geothermal Reservoir Studies," *Geothermal Research Council, Transactions, 8*, 1984 pp. 349-354.